

Perpendicular electric field drives Chern transitions and layer polarization changes in Hofstadter bands

Pratap Chandra Adak^{1,*}, Subhajit Sinha¹, Debasmita Giri², Dibya Kanti Mukherjee^{3,4,5}, Chandan¹, L. D. Varma Sangani¹, Surat Layek¹, Ayshi Mukherjee¹, Kenji Watanabe⁶, Takashi Taniguchi⁷, H.A. Fertig^{3,4}, Arijit Kundu^{2,*}, and Mandar M. Deshmukh^{1,*}

¹*Department of Condensed Matter Physics and Materials Science, Tata Institute of Fundamental Research, Homi Bhabha Road, Mumbai 400005, India.*

²*Department of Physics, Indian Institute of Technology, Kanpur 208016, India.*

³*Department of Physics, Indiana University, Bloomington, IN 47405.*

⁴*Quantum Science and Engineering Center, Indiana University, Bloomington, IN, 47408.*

⁵*Laboratoire de Physique des Solides, Univ. Paris-Sud, Université Paris Saclay, CNRS, UMR 8502, F-91405 Orsay Cedex, France.*

⁶*Research Center for Functional Materials, National Institute for Materials Science, 1-1 Namiki, Tsukuba 305-0044, Japan.*

⁷*International Center for Materials Nanoarchitectonics, National Institute for Materials Science, 1-1 Namiki, Tsukuba 305-0044, Japan.*

*pratapchandraadak@gmail.com, kundua@iitk.ac.in, deshmukh@tifr.res.in

Abstract

Moiré superlattices engineer band properties and enable observation of fractal energy spectra of Hofstadter butterfly. Recently, correlated-electron physics hosted by flat bands in small-angle moiré systems has been at the foreground. However, the implications of moiré band topology within the single-particle framework are little explored experimentally. An outstanding problem is understanding the effect of band topology on Hofstadter physics, which does not require electron correlations. Our work experimentally studies Chern state switching in the Hofstadter regime using twisted double bilayer graphene (TDBG), which offers electric field

tunable topological bands, unlike twisted bilayer graphene. Here we show that the nontrivial topology reflects in the Hofstadter spectra, in particular, by displaying a cascade of Hofstadter gaps that switch their Chern numbers sequentially while varying the perpendicular electric field. Our experiments together with theoretical calculations suggest a crucial role of charge polarization changing concomitantly with topological transitions in this system. Layer polarization is likely to play an important role in the topological states in few-layer twisted systems. Moreover, our work establishes TDBG as a novel Hofstadter platform with nontrivial magnetoelectric coupling.

Introduction

The 2D moiré lattice, when subjected to a magnetic field, loses its periodicity due to spatial dependence of the gauge potential. However, when the applied magnetic field is such that the magnetic flux quantum per unit cell of the moiré lattice is a rational number, the discrete translational symmetry of the lattice is restored with a larger magnetic unit cell. The energy spectrum of such a system, as a function of the magnetic field, has a self-similar fractal structure known as Hofstadter's butterfly¹. The observation of this quantum fractal is limited by the requirement of high magnetic flux Φ through the unit cell, such that $\Phi/\Phi_0 \sim 1$. Here, $\Phi_0 = h/e$ is the magnetic flux quantum, with h being Planck's constant and e being the electron charge. Hofstadter's butterfly was first observed in graphene aligned to hexagonal boron nitride (hBN)^{2,3}. The large unit cell in such moiré superlattices realizes $\Phi/\Phi_0 \sim 1$ with available lab magnets.

Recently, the ability to stack multiple layers of 2D materials rotated with sub-degree precision has opened up a new frontier. In addition to tuning the moiré length scale, the twist angle between two adjacent layers tunes the symmetry and the topology of the emergent moiré bands, providing new experimental knobs. Furthermore, magic-angle twisted bilayer graphene (TBG) hosts low-energy flat bands⁴⁻⁶ that support correlated-electron phenomena such as correlated insulator states⁷⁻⁹, ferromagnetism^{10,11}, and superconductivity^{9,12}. Topological properties of the twisted systems are of particular interest, as several recent studies have explored correlated Chern insulator states in the Hofstadter regime in TBG¹³⁻¹⁸. These states are interpreted as arising due to the occupation of subsets of underlying Chern bands¹³⁻¹⁵ or Hofstadter subbands¹⁶⁻¹⁸, a mechanism similar to Quantum Hall ferromagnetism. In the physics of Chern insulator states, as also in the quantum

Hall physics due to the formation of Landau levels, gaps with different Chern numbers can be accessed by changing the Fermi energy by varying the charge density. Recently a pure electrical control, such as the perpendicular electric field, to open up a Chern insulating state from a bulk gapless state has been demonstrated using a correlated system¹⁹. Similar electrical control over Chern states without requiring electron correlation will be novel.

Twisted double bilayer graphene (TDBG), made by twisting two copies of Bernal stacked bilayer graphene (BLG), provides such opportunities as the electric field can tune the band structure and its topological properties^{20–26}. Notably, the flat bands in TDBG possess a nonzero valley Chern number that changes with the electric field, offering a unique correlated Hofstadter platform²⁷. While earlier experiments in TDBG have a major focus on electron correlations physics^{28–34}, the tunability of the topological flat bands in the Hofstadter regime is little explored³⁵. An ability to tune the Chern numbers of these bands would provide further insight on the role of topology in these correlated states. Thus TDBG is a rich platform as the electric field plays an important role, unlike in TBG.

In this work, we study electron transport in TDBG with small twist angles around 1.1° - 1.5° under a high magnetic field upto $\Phi/\Phi_0 \sim 1/3$. We observe a cascade of gaps that change their Chern numbers sequentially as the perpendicular electric field is varied. This contrasts with TBG for which the band structure is unaffected by such an electric field, and so cannot induce Chern transition. The Hofstadter fan diagrams we measure show additional features that reveal the topological nature of the underlying band structure. Our calculation of the Hofstadter energy spectrum in TDBG confirms the key experimental observations. Interestingly, we find that a small exchange enhanced spin Zeeman term plays a role in determining the sequence of Chern gaps. Furthermore, our analysis shows that the electric field varies the layer polarization and provides the underlying mechanism of the Chern transition.

Results

Low-temperature transport. We now present our magneto-transport measurements in TDBG devices. To fabricate TDBG devices, we cut two pieces of BLG from a single exfoliated flake and sandwich them between two hBN flakes with a relative rotation³⁶. A schematic of our device

structure is shown in Fig. 1a. Using the metal top gate and Si^{++} bottom gate we can independently control the charge density, n , and the perpendicular electric displacement field, D . Using the multiple electrodes in the devices we measure low-temperature electron transport in a Hall bar geometry under a perpendicular magnetic field, B . See Methods section for details about fabrication and measurement.

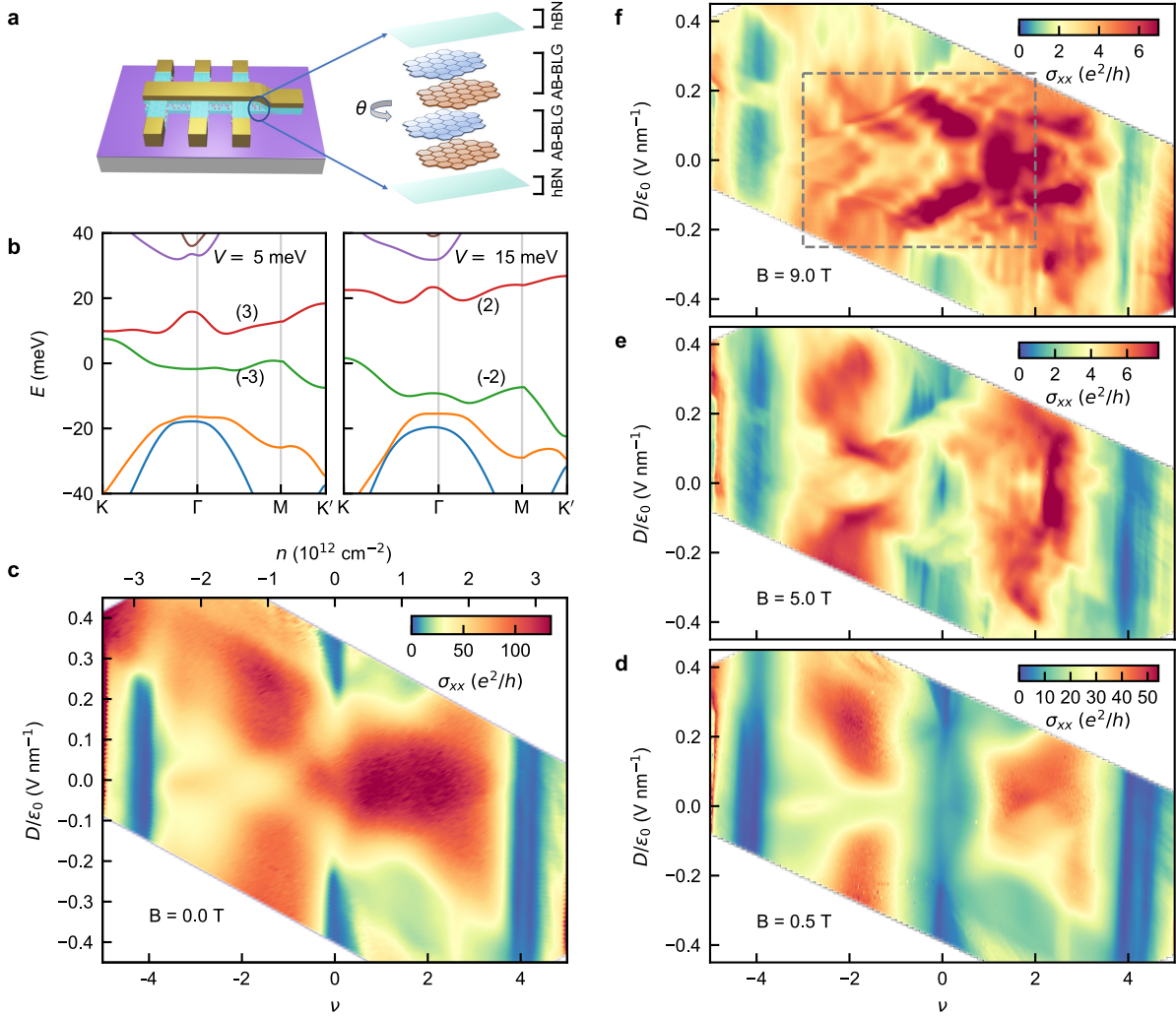


Fig. 1: Magneto-transport in twisted double bilayer graphene (TDBG). **a** Schematic of the dual gated TDBG device. **b** Calculated band structure for TDBG with twist angle 1.10° in absence of the magnetic field for two different values of the interlayer potential V . Interlayer potential simulates the application of the electric field. The numbers in brackets adjacent to each band indicate the corresponding valley Chern number, which changes with V . **c** σ_{xx} as a function of moiré filling ν and perpendicular electric displacement field D at zero magnetic field at 300 mK. **d-f** Variation of σ_{xx} vs. ν and D at three different values of perpendicular magnetic field, B . The region inside the dashed rectangle in **f** is discussed in details in Fig. 2.

We first discuss electron transport in zero magnetic field. In Fig. 1b, we calculate the zero magnetic field band structures of TDBG with a twist angle of 1.10° for two different electric fields

(see Supplementary Note 1 for calculation details). In addition to the tunability of the band gaps and width, the valley Chern numbers of the moiré bands change with the electric field. In Fig. 1c, we show a color-scale plot of the longitudinal conductivity, σ_{xx} , as a function of ν and D at $B = 0$ T and a temperature of 300 mK for a TDBG device with twist angle 1.10° . Here, $\nu = 4n/n_S$ is the moiré filling factor, where n_S is the number of charge carriers required to fill an isolated moiré band and the factor 4 incorporates the spin and valley degeneracy. In the color-scale plot of σ_{xx} , conductivity dips are observed corresponding to two moiré gaps at $\nu = \pm 4$ and the CNP gap at $\nu = 0$. The electric field tunability of the underlying band structure is evident as two moiré gaps close at a high electric field, and the CNP gap opens up only above a finite electric field value. We also see additional regions with low conductance – a cross-like feature around $D/\epsilon_0 = 0$ and $\nu \sim -2$ on the hole side and two halo regions around $D/\epsilon_0 = \pm 0.3$ V/nm and $\nu \sim 2$ on the electron side. These are characteristic features of small-angle TDBG³⁷. Here we note, while the correlated gaps at partial filling develop in TDBG with twist angle $\sim 1.2^\circ - 1.4^\circ$, for smaller twist angle $\sim 1.1^\circ$ correlated gaps develop under a parallel magnetic field^{23,28,30}. See Supplementary Fig. 8 for data from a 1.46° device, where we observe correlated gap at a zero magnetic field.

Observation of electric field tunable Chern gaps in high magnetic field. To study the effect of a perpendicular magnetic field B , we now measure σ_{xx} as a function of ν and D for different values of B as shown in Fig. 1d-f. In contrast to the case of $B = 0$, the CNP gap emerges even at $D = 0$ as we apply a finite magnetic field (see Fig. 1d). Furthermore, as evident from the σ_{xx} plot at 5 T in Fig. 1e, the CNP gap undergoes multiple closing and reopening as the electric field is varied. At higher magnetic fields, such as at 9 T in Fig. 1f, the formation of Landau Levels (LL) leads to multiple lines of conductivity peaks and dips parallel to the D -axis. Our most interesting observation is that the positions of the σ_{xx} dips shift discretely on the ν -axis as the electric field is varied. This effect of the electric field is most prominent in the region $|D|/\epsilon_0 \lesssim 0.25$ V/nm (indicated by the dashed rectangle in Fig. 1f). Interestingly, within this D -range, marked by the closing of the hole-side moiré gap at $|D|/\epsilon_0 \sim 0.25$ V/nm at zero magnetic field, both the flat bands are isolated from the remote moiré bands. At higher electric fields, as the flat bands merge with the remote moiré bands, the electric field tunability becomes weaker.

We now study the step-like evolution of the σ_{xx} dips with D in detail by focusing on σ_{xx} as a function of ν and D at $B = 9$ T in Fig. 2a. To elucidate the nature of these dips as they

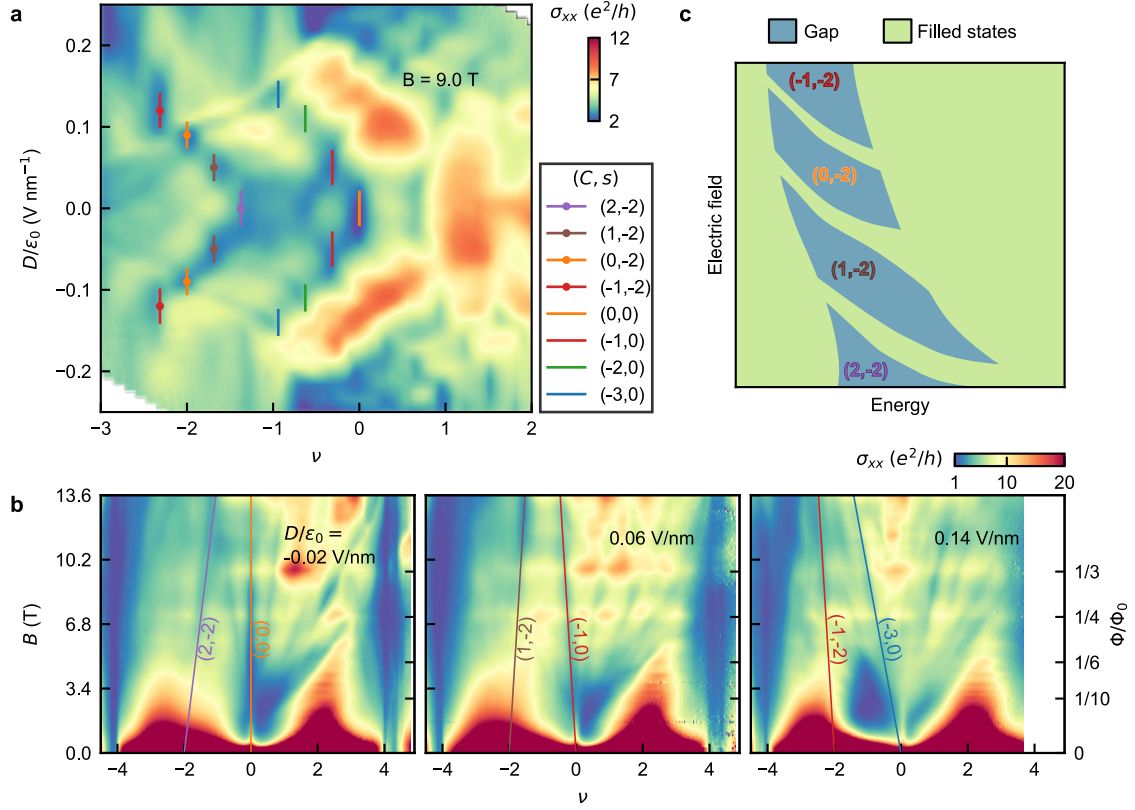


Fig. 2: Electric field tunable Chern gaps. **a** Color-scale plot of σ_{xx} as a function ν and D at $B = 9$ T. The overlaid lines of different colors indicate the (C, s) values of the corresponding σ_{xx} dips as in the legend. (C, s) values are inferred from **b** with C being the Chern number and s being the moiré filling factor corresponding to $B = 0$ T (see Supplementary Fig. 6 for fitting details to extract (C, s) values). **b** Color-scale plots of σ_{xx} as a function of ν and B , i.e., fan diagrams, at three different values of D . The overlaid lines trace the trajectory of the σ_{xx} minima. The slope and the ν -axis intercept give C and s , respectively. (C, s) values are indicated adjacent to the lines and assigned in **a** accordingly. **c** Schematic representation of the origin of electric field tunable Chern gaps. Chern number of the gaps changes when Hofstadter subbands with Chern number 1 peel off from a group of Hofstadter subbands and merge with another group as the electric field is varied.

evolve in the three-dimensional parameter space of ν , D , and B , we perform a systematic analysis. We first identify two groups of most prominent σ_{xx} dips corresponding to the larger gaps (see the Supplementary Note 3 and Supplementary Fig. 2 for estimation of the gaps), which shift further on the hole side as D is increased, by line segments of different colors. Then to track the evolution of these dips with B , we measure σ_{xx} as a function of ν and B at different values of constant D . In Fig. 2b, we show three such plots, namely fan diagrams, for three different D . We focus on the pair of prominent σ_{xx} dips in each fan diagram. The position of the dips on the ν -axis evolve with B along linear trajectories marked with lines of the same colors as in Fig. 2a. Besides the marked pair of dips, there are other dips which are also tuned by the electric field (Supplementary Fig. 4).

See Supplementary Note 4 and Supplementary Figs. 7-9 for similar data from devices with different twist angles.

The linear trajectories of the conductivity dips can be understood in terms of Hofstadter physics. Within the Hofstadter picture, the gaps with integer Chern number C follow linear trajectories in n - B diagram, i.e., the Wannier diagram, given by the Diophantine equation,

$$\nu = C \frac{\Phi}{\Phi_0} + s. \quad (1)$$

Here, s is an integer denoting the moiré filling factor corresponding to the number of carriers per moiré unit cell in zero magnetic field, and $\Phi = BA$, with A being the area of the moiré unit cell. We extract C and s from the slope and ν -axis intercept in the fan diagrams at different D for all the marked lines. The extracted values of (C, s) are marked in Fig. 2b. Then we assign these (C, s) values inferred from Fig. 2b to the corresponding σ_{xx} minima in Fig. 2a. Here we note that from the evolution of σ_{xx} dips with temperature we extract the Hofstadter gaps to be $\sim 0.1 - 0.5$ meV (see Supplementary Note 3 and Supplementary Fig. 2). Our experimental data of σ_{xy} (Supplementary Fig. 5) show weak quantization possibly due to the smallness of these gaps together with angle inhomogeneity disorder³⁸. See Supplementary Note 6 and Supplementary Fig. 11 for the role of flat band energy scale in Hofstadter spectra. Also, moiré commensurability aspects can lead to absence of quantization³⁹.

From Fig. 2a, we find two interesting trends in the transition of (C, s) as a function of D . Firstly, for both the groups corresponding to $s = 0$ and $s = -2$, the Chern number decreases sequentially by 1 as the magnitude of D is increased; crucially, we observe both even and odd Chern numbers. Secondly, the difference in C for $s = 0$ and $s = -2$ remains 2. The sequential change of Chern number by D can be empirically understood by considering a simple schematic in Fig. 2c, where a part of the Chern band peels off due to varying electric field. As D is varied, branches with Chern number 1 are separated from a group of Hofstadter subbands and merge with another group, resulting in a sequence of Chern gaps with different C . A dip in σ_{xx} , observed experimentally, corresponds to a gap between two groups of Hofstadter subbands. This simple picture of the sequential evolution of the Chern gaps with electric field as Hofstadter subbands peel off is confirmed by our theoretical calculation which we discuss next.

Calculation of Hofstadter spectra in TDBG. To calculate the Hofstadter energy spectrum in TDBG, we construct a Hamiltonian for each valley in the basis of bare Landau levels of graphene, indexed by the Landau level index, guiding center, and layer index. Inter-bilayer tunneling then couples states with various guiding centers and Landau levels of each layer and one can diagonalize the Hamiltonian to find the spectra. The prominent Chern gaps are characterized as a function of the filling factor ν , calculated from the charge neutrality point and flux quanta per moiré unit cell, Φ/Φ_0 , obtained by solving the Diophantine equation (Eq.1). In Fig. 3a, we plot the Hofstadter spectra for both K and K' valleys in two different colors for an interlayer potential of $V = 20$ meV. Here we note that at nonzero V the valley degeneracy is already lifted due to the nontrivial topology of the underlying band structure, as we discuss later. The observation of odd Chern numbers further implies that the spin degeneracy is also lifted. To incorporate this in our calculation we include an exchange enhanced spin Zeeman term $\Delta_S = 2.5$ meV; such term can arise due to electron correlations of the flat bands. See Supplementary Note 2 for the details of the calculation. In Fig. 3b, we plot the Wannier diagram showing the evolution of the Chern gaps as a function of ν and Φ/Φ_0 for $V = 20$ meV. Here the width of the line segments indicates the strength of the corresponding gaps considering both K and K' valleys. See Supplementary Fig. 1 for calculation at other electric field values. Similar to our experimental observation, we find that two prominent Chern gaps originate from $s = 0$ and $s = -2$ and their Chern numbers change with the electric field.

To further elucidate the electric field-induced quantum phase transition of Chern numbers we plot the evolution of the Hofstadter energy spectrum as a function of the inter-layer potential V at a constant $\Phi/\Phi_0 = 0.32 \sim B = 9$ T in Fig. 3c. We find that the energy levels disperse nonmonotonically with V . As a result, branches of a Chern band peel off and merge with another band, giving rise to gaps with different Chern numbers at different electric fields. The corresponding plot of extracted Chern gaps as a function ν and V is shown in Fig. 3d. Interestingly, the sequence of changes in the prominent Chern gaps in Fig. 3d match quite well with our experimental data in Fig. 2a. Moreover, the Chern gaps are more prominent on the hole side, again as seen in experiment.

Role of electric field-tunable layer polarization. To understand the underlying mechanism further, we now discuss the role of an induced layer polarization in tuning the Hofstadter spectra. Under an applied electric field, electrons occupying the four different layers of TDBG are at different values of on-site potential, V_i , $i = 1, 2, 3, 4$. This contributes a mean-field energy of the form

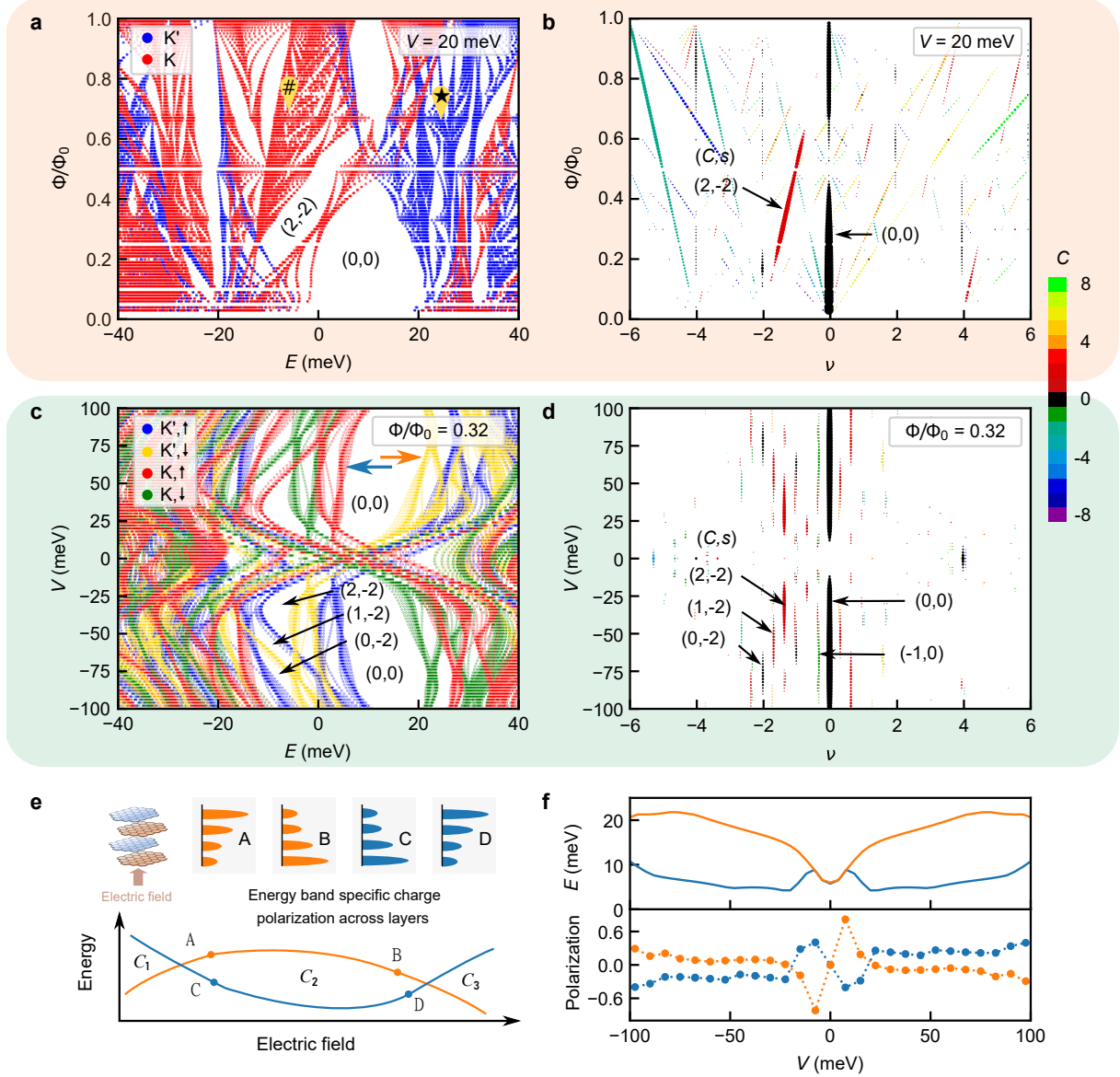


Fig. 3: Calculation of Hofstadter spectra and layer polarization in TDBG. **a** Calculated Hofstadter energy levels for both K and K' valleys in TDBG with twist angle 1.10° for an interlayer potential of $V = 20$ meV. Energy levels disperse differently for two valleys due to different topology resulting in fewer number of gaps—e.g., energy gap for K valley at location \star is filled with energy levels from K' valley (vice versa for location $\#$). **b** Corresponding Wannier diagram showing the evolution of Hofstadter gaps considering both the valleys as a function ν and Φ/Φ_0 . **c** Evolution of energy spectra as a function of interlayer potential V at a constant magnetic field corresponding to $\Phi/\Phi_0 = 0.32 \sim 9$ T with an exchange enhanced Zeeman splitting of 2.5 meV. This confirms the change in Chern numbers as schematically depicted in Fig. 2c. **d** Evolution of gaps as a function of ν and V extracted from **c**. The width of the line segments in **b** and **d** are proportional to the values of the gaps in the Hofstadter spectrum. The color of the line segments denotes the corresponding Chern number C , as indicated in the color-scale legend. **e** Schematic depicting the role of energy band-specific charge polarization across layers in energy vs. electric field dispersion. When electrons are polarized more toward top (bottom) layers, as for points A and D (B and C), the energy of the band increases (decreases) with increasing electric field. As the layer polarization is varied by the electric field, energy disperses nonmonotonically with the electric field inducing multiple gap closing and opening—this can lead to changes in the Chern number of the gap. **f** Calculated layer polarization (bottom panel) corresponding to two Hofstadter bands (top panel) across the CNP gap (0,0) (indicated by two arrows in **c**). Panels **a** and **b** are shaded in the same color to indicate that they are extracted from the same data (similarly for panels **c** and **d**).

$E \sim \sum \rho_i V_i$, where ρ_i is the electron density of i -th layer. As V_i changes proportionally with the electric field, the nonmonotonic change in E with the electric field in Fig. 3c suggests an asymmetric change in the distribution of ρ_i . To measure the asymmetric change in the distribution, we define an energy band specific charge polarization across layers, $P = \rho_1 + \rho_2 - \rho_3 - \rho_4$. The role of this layer polarization in determining the energy vs. electric field dispersion is depicted schematically in Fig. 3e. For an electron distribution polarized toward the top layer, the energy increases with an increasing electric field, and hence the energy vs. electric field dispersion has a positive slope. The slope is negative for the opposite polarization. As the layer polarization is varied by the electric field, the energy state evolves nonmonotonically with the electric field. When two energy bands with different Chern numbers cross each other, the Chern number of the gap between the two bands changes. The electric field tunable layer polarization is indeed confirmed in Fig. 3f where we plot the polarization vs. V for two different energy levels across the CNP.

Fig. 3e further suggests how the tunable layer polarization can manifest itself into a complex evolution of a gap, with the possibility of multiple closings and reopenings⁴⁰. Indeed, we verify this interesting implication as we measure σ_{xx} at the CNP gap as a function of B and D . We find a complex evolution of the CNP gap with multiple closings and reopenings, a feature distinct from other materials like BLG, suggesting important role of field tunable layer polarization in twisted systems (details in the Supplementary Note 5 and Supplementary Fig. 10).

Role of topology on Hofstadter spectra. Finally, we discuss the important role of the nontrivial topology of the TDBG band structure in determining the Hofstadter spectra. At finite values of the electric field, the valley Chern numbers of K and K' valleys are nonzero and opposite in sign. As seen from Fig. 3a, the Hofstadter energy spectra from two valleys disperse differently with the magnetic field due to the different topologies of the two valleys²⁷. This has two important implications. Firstly, the two-fold valley degeneracy is lifted, as we noted earlier. Secondly, only the most prominent gaps survive as gaps in the Hofstadter spectrum of one valley can be filled by the energy states of the other. This is evidenced in our experimental data as well.

We find additional signatures of the nontrivial band topology in the Hofstadter energy spectra in TDBG. The Hofstadter spectrum of a topologically trivial band is confined within the band, i.e., disconnected from the spectra of the neighboring bands. Conversely, the Hofstadter spectrum of a topological band connects to that of a nearby band, such that the total Chern number of the bands

with connected Hofstadter spectra is zero^{41,42}. Consequently, in a Hofstadter energy spectrum for a topological band, the gap with a nonzero Chern number C closes at $\Phi/\Phi_0 \leq 1/|C|$. Indeed, our calculation in Fig. 3a-b confirms this as the CNP gap $(0,0)$ closes at $\Phi/\Phi_0 < 0.5$, consistent with valley Chern number 2 at the CNP gap of AB-AB TDBG at a finite electric field. This contrasts with the Hofstadter spectrum for AB-BA TDBG at a finite electric field, for which the CNP gap has a zero valley Chern number, and find the CNP gap open throughout $0 < \Phi/\Phi_0 < 1$ (Fig. 4a-b).

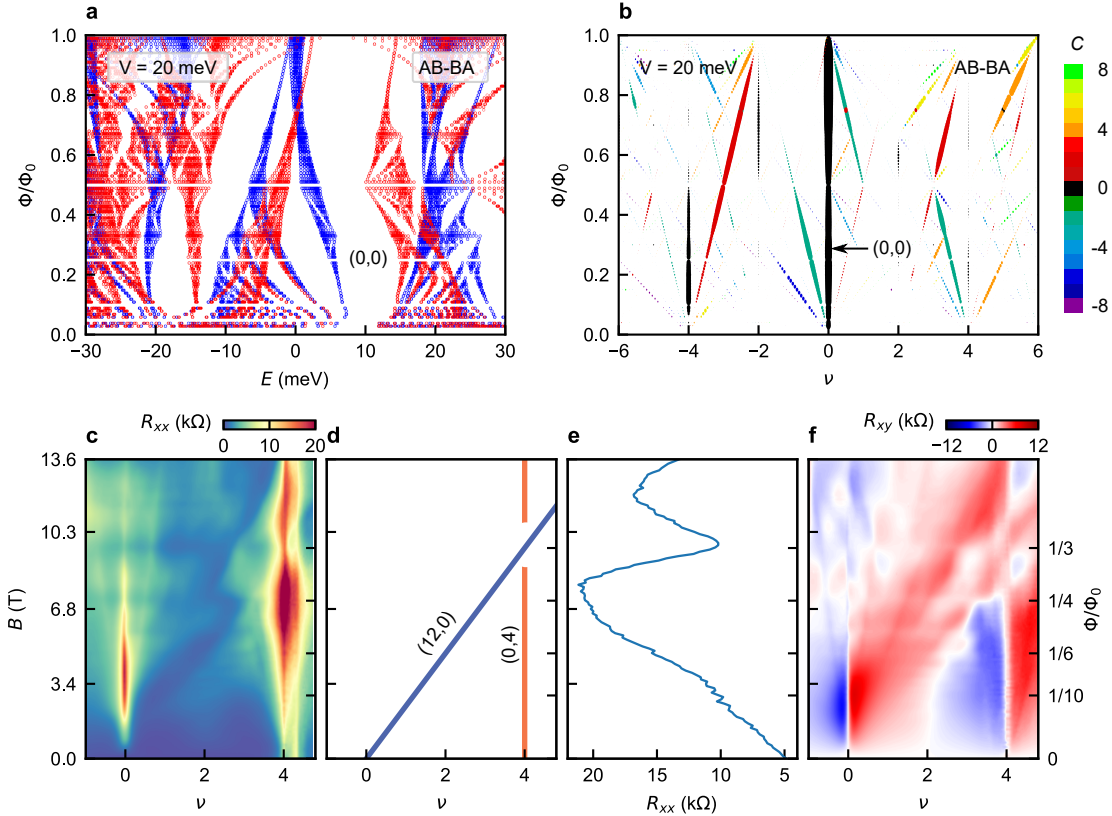


Fig. 4: Role of topology on Hofstadter spectra. **a** Calculated Hofstadter energy levels for both K (red) and K' (blue) valleys in AB-BA TDBG with twist angle 1.10° for an interlayer potential of $V = 20$ meV. **b** Evolution of gaps corresponding to the spectrum in **a**. Unlike AB-AB case (see Fig. 3a-b), the CNP gap $(0,0)$ is open for any flux $0 < \Phi/\Phi_0 < 1$. **c** Color-scale plot of R_{xx} as a function ν and B at $D/\epsilon_0 = -0.02$ V/nm from the 1.10° AB-AB TDBG device. **d** Schematic of **c**, showing the weakening of the moiré gap $(0,4)$ at $\Phi/\Phi_0 = 1/3$ when a Hofstadter gap $(12,0)$ crosses. **e** Line slices of R_{xx} vs. B at $\nu = 4$ showing a clear dip at the crossing. **f** Color-scale plot of R_{xy} corresponding to **c**. The Hofstadter gap $(12,0)$ (with finite R_{xy}) dominates over the moiré gap $(0,4)$ (zero R_{xy}), indicating that Hofstadter spectra across the moiré gap are connected to each other.

To see experimental signatures of nontrivial band topology, we plot R_{xx} as a function of ν and B for $D/\epsilon_0 = -0.02$ V/nm in Fig. 4c from the 1.10° AB-AB TDBG device. We find that the moiré gap of $\nu = 4$ is weakened at $\Phi/\Phi_0 = 1/3$, as the Hofstadter gap of $(12,0)$ crosses it (also see Fig. 4e for a line-plot of R_{xx} vs. B at $\nu = 4$). The nonzero R_{xy} at the crossing point of the moiré gap,

where R_{xy} is otherwise zero, further corroborates the dominance of the Hofstadter gap of (12,0) over the moiré gap of (0,4) (Fig. 4f). This suggests that the Hofstadter spectra across the moiré gap are connected due to the nontrivial topology.

Discussion

In conclusion, we have presented a comprehensive study of magneto-transport in TDBG in Hofstadter regime, complemented by theoretical calculations of Hofstadter spectra. We identified the manifestation of underlying nontrivial topology of the TDBG flat bands on these spectra. The tunable layer polarization plays a key role in determining the Hofstadter spectra and the quantum phase transition between Chern gaps.

Our central result, that the Chern gap can be controlled by varying the electric field, rather than the charge density, has important implications for magnetoelectric coupling: a Chern gap Δ_g with Chern number C gives rise to a change in magnetization, $\delta M \propto C\Delta_g$ ⁴³. Thus the physics we have identified allows electrical control of the system magnetization. Here we note that the control over Chern states has been recently demonstrated in twisted monolayer-bilayer graphene by tuning the charge density⁴⁴ and in hBN-aligned ABC trilayer graphene using the electric field¹⁹. Our work demonstrates a novel pathway to control Chern states using the electric field without requiring electron correlation as a prerequisite. Furthermore, the Hofstadter platform of TDBG offers a plethora of Chern transitions over a broad region of electric field. It is interesting to speculate that ferroelectric correlations, as seen in recent experiments⁴⁵, could stabilize Chern bands and the physics we discuss in this study even at zero magnetic field.

Methods

Device fabrication

To fabricate TDBG devices, we first exfoliated graphene flakes and cut the selected bilayer graphene flake into two halves by using a scalpel made from an optical fiber³⁶. The bilayer graphene flakes were chosen based on optical contrast and later confirmed by Raman spectroscopy. We chose exfoliated hBN flakes of 20 nm to 40 nm in thickness, first based on optical inspection of the color

and later measured by AFM. Then we made the hBN-BLG-BLG-hBN stack using the standard poly-carbonate (PC) based dry transfer method⁴⁶ and dropped on SiO₂/Si⁺⁺ substrate. The twist angle was introduced by rotating the bottom stage while picking up the second half of the bilayer graphene flake. Afterward, we made the top gate by e-beam lithography and depositing Cr/Au by e-beam evaporation. Subsequently, we defined the geometry of the devices by e-beam lithography followed by etching in CHF₃+O₂ plasma. Finally, we made 1D edge contact by etching in CHF₃+O₂ plasma and then depositing Cr/Pd/Au.

Transport measurement

We carried out the low-temperature transport measurements at 300 mK in a He-3 insert inside a liquid He flow cryostat under a perpendicular magnetic field from 0 T to 13.6 T. A current of ~ 10 nA was sent, and the four-probe voltage was measured using lock-in amplifier using low frequency (~ 13 -17 Hz) after amplifying with a preamplifier. The measurement of the magneto-resistance at the CNP gap presented in Supplementary Fig. 10 was carried out at 20 mK in a dilution fridge upto $B = 12$ T. The charge density n and the perpendicular electric displacement field D were calculated using the formula, $n = (C_{BG}V_{BG} + C_{TG}V_{TG})/e - n_0$ and $D = (C_{BG}V_{BG} - C_{TG}V_{TG})/2 - D_0$. Here C_{TG} and C_{BG} are the capacitance per unit area of the top and the back gate, respectively, e being the charge of an electron. n_0 and D_0 are the small offsets in the charge density and the electric displacement field. The capacitance values were calculated at first by noting the dielectric thickness and later estimated more precisely using the magneto-transport features such as the positions of the Brown-Zak oscillations on B -axis. To avoid artifacts associated with lead asymmetry we symmetrize the longitudinal resistance as $\bar{R}_{xx}(B) = (R_{xx}(B) + R_{xx}(-B))/2$, and antisymmetrize the transverse resistance as $\bar{R}_{xy}(B) = (R_{xy}(B) - R_{xy}(-B))/2$. The longitudinal conductivity σ_{xx} and the transverse conductivity σ_{xy} were calculated using the formula $\sigma_{xx} = (w/l)\bar{R}_{xx}/(\bar{R}_{xy}^2 + (w/l)^2\bar{R}_{xx}^2)$ and $\sigma_{xy} = \bar{R}_{xy}/(\bar{R}_{xy}^2 + (w/l)^2\bar{R}_{xx}^2)$, respectively. Here, w is the width and l is the length of the Hall bar geometry. In the text, the symmetrized longitudinal resistance and the antisymmetrized transverse resistance are denoted by R_{xx} and R_{xy} for brevity.

Twist angle determination

We determine the twist angle θ based on our low-temperature electron transport measurement, using the relation $n_S = 8\theta^2/\sqrt{3}a^2$. Here n_S is the charge carrier density corresponding to the full filling of the moiré band ($\nu = \pm 4$), $a = 0.246$ is the lattice constant of graphene. To determine n_S , we locate $\nu = \pm 4$ by tracing the sequence of Landau levels to the n -axis at $B = 0$.

Data Availability

The experimental data used in the figures of the main text are available in Zenodo with the identifier [doi:10.5281/zenodo.5653688](https://doi.org/10.5281/zenodo.5653688)⁴⁷. Additional data related to this study are available from the corresponding authors upon reasonable request.

References

- [1] Hofstadter, D. R. Energy levels and wave functions of Bloch electrons in rational and irrational magnetic fields. *Physical Review B* **14**, 2239–2249 (1976).
- [2] Hunt, B. *et al.* Massive Dirac Fermions and Hofstadter Butterfly in a van der Waals Heterostructure. *Science* **340**, 1427–1430 (2013).
- [3] Dean, C. R. *et al.* Hofstadter’s butterfly and the fractal quantum Hall effect in moiré superlattices. *Nature* **497**, 598–602 (2013).
- [4] Suárez Morell, E., Correa, J. D., Vargas, P., Pacheco, M. & Barticevic, Z. Flat bands in slightly twisted bilayer graphene: Tight-binding calculations. *Physical Review B* **82**, 121407 (2010).
- [5] Lopes dos Santos, J. M. B., Peres, N. M. R. & Castro Neto, A. H. Continuum model of the twisted graphene bilayer. *Physical Review B* **86**, 155449 (2012).
- [6] Bistritzer, R. & MacDonald, A. H. Moiré bands in twisted double-layer graphene. *Proceedings of the National Academy of Sciences* **108**, 12233–12237 (2011).
- [7] Kim, K. *et al.* Tunable moiré bands and strong correlations in small-twist-angle bilayer graphene. *Proceedings of the National Academy of Sciences* **114**, 3364–3369 (2017).

- [8] Cao, Y. *et al.* Correlated insulator behaviour at half-filling in magic-angle graphene superlattices. *Nature* **556**, 80–84 (2018).
- [9] Cao, Y. *et al.* Unconventional superconductivity in magic-angle graphene superlattices. *Nature* **556**, 43–50 (2018).
- [10] Sharpe, A. L. *et al.* Emergent ferromagnetism near three-quarters filling in twisted bilayer graphene. *Science* **365**, 605–608 (2019).
- [11] Serlin, M. *et al.* Intrinsic quantized anomalous Hall effect in a moiré heterostructure. *Science* **367**, 900–903 (2020).
- [12] Lu, X. *et al.* Superconductors, orbital magnets and correlated states in magic-angle bilayer graphene. *Nature* **574**, 653–657 (2019).
- [13] Nuckolls, K. P. *et al.* Strongly correlated Chern insulators in magic-angle twisted bilayer graphene. *Nature* **588**, 610–615 (2020).
- [14] Das, I. *et al.* Symmetry-broken Chern insulators and Rashba-like Landau-level crossings in magic-angle bilayer graphene. *Nature Physics* **17**, 710–714 (2021).
- [15] Wu, S., Zhang, Z., Watanabe, K., Taniguchi, T. & Andrei, E. Y. Chern insulators, van Hove singularities and topological flat bands in magic-angle twisted bilayer graphene. *Nature Materials* **20**, 488–494 (2021).
- [16] Saito, Y. *et al.* Hofstadter subband ferromagnetism and symmetry-broken Chern insulators in twisted bilayer graphene. *Nature Physics* **17**, 478–481 (2021).
- [17] Park, J. M., Cao, Y., Watanabe, K., Taniguchi, T. & Jarillo-Herrero, P. Flavour Hund’s coupling, Chern gaps and charge diffusivity in moiré graphene. *Nature* **592**, 43–48 (2021).
- [18] Choi, Y. *et al.* Correlation-driven topological phases in magic-angle twisted bilayer graphene. *Nature* **589**, 536–541 (2021).
- [19] Chen, G. *et al.* Tunable correlated Chern insulator and ferromagnetism in a moiré superlattice. *Nature* **579**, 56–61 (2020).

- [20] Chebrolu, N. R., Chittari, B. L. & Jung, J. Flat bands in twisted double bilayer graphene. *Physical Review B* **99**, 235417 (2019).
- [21] Zhang, Y.-H., Mao, D., Cao, Y., Jarillo-Herrero, P. & Senthil, T. Nearly flat Chern bands in moiré superlattices. *Physical Review B* **99**, 075127 (2019).
- [22] Koshino, M. Band structure and topological properties of twisted double bilayer graphene. *Physical Review B* **99**, 235406 (2019).
- [23] Lee, J. Y. *et al.* Theory of correlated insulating behaviour and spin-triplet superconductivity in twisted double bilayer graphene. *Nature Communications* **10**, 5333 (2019).
- [24] Choi, Y. W. & Choi, H. J. Intrinsic band gap and electrically tunable flat bands in twisted double bilayer graphene. *Physical Review B* **100**, 201402(R) (2019).
- [25] Liu, J., Ma, Z., Gao, J. & Dai, X. Quantum Valley Hall Effect, Orbital Magnetism, and Anomalous Hall Effect in Twisted Multilayer Graphene Systems. *Physical Review X* **9**, 031021 (2019).
- [26] Wang, Y.-X., Li, F. & Zhang, Z.-Y. Phase diagram and orbital Chern insulator in twisted double bilayer graphene. *Physical Review B* **103**, 115201 (2021).
- [27] Crosse, J. A., Nakatsuji, N., Koshino, M. & Moon, P. Hofstadter butterfly and the quantum Hall effect in twisted double bilayer graphene. *Physical Review B* **102**, 035421 (2020).
- [28] Burg, G. W. *et al.* Correlated Insulating States in Twisted Double Bilayer Graphene. *Physical Review Letters* **123**, 197702 (2019).
- [29] Shen, C. *et al.* Correlated states in twisted double bilayer graphene. *Nature Physics* **16**, 520–525 (2020).
- [30] Adak, P. C. *et al.* Tunable bandwidths and gaps in twisted double bilayer graphene on the verge of correlations. *Phys. Rev. B* **101**, 125428 (2020).
- [31] Cao, Y. *et al.* Tunable correlated states and spin-polarized phases in twisted bilayer–bilayer graphene. *Nature* **583**, 215–220 (2020).

- [32] Liu, X. *et al.* Tunable spin-polarized correlated states in twisted double bilayer graphene. *Nature* **583**, 221–225 (2020).
- [33] Sinha, S. *et al.* Bulk valley transport and Berry curvature spreading at the edge of flat bands. *Nature Communications* **11**, 5548 (2020).
- [34] Liu, L. *et al.* Isospin competitions and valley polarized correlated insulators in twisted double bilayer graphene. *Nature Communications* **13**, 3292 (2022).
- [35] Burg, G. W. *et al.* Evidence of Emergent Symmetry and Valley Chern Number in Twisted Double-Bilayer Graphene. Preprint at <https://arxiv.org/abs/2006.14000> (2020).
- [36] Sangani, L. D. V. *et al.* Facile deterministic cutting of 2D materials for twistrionics using a tapered fibre scalpel. *Nanotechnology* **31**, 32LT02 (2020).
- [37] He, M. *et al.* Symmetry breaking in twisted double bilayer graphene. *Nature Physics* **17**, 26–30 (2021).
- [38] Tschirhart, C. L. *et al.* Imaging orbital ferromagnetism in a moiré Chern insulator. *Science* **372**, 1323–1327 (2021).
- [39] Shi, J., Zhu, J. & MacDonald, A. H. Moiré commensurability and the quantum anomalous Hall effect in twisted bilayer graphene on hexagonal boron nitride. *Physical Review B* **103**, 075122 (2021).
- [40] Sanchez-Yamagishi, J. D. *et al.* Quantum Hall Effect, Screening, and Layer-Polarized Insulating States in Twisted Bilayer Graphene. *Physical Review Letters* **108**, 076601 (2012).
- [41] Lian, B., Xie, F. & Bernevig, B. A. Landau level of fragile topology. *Physical Review B* **102**, 041402 (2020).
- [42] Herzog-Arbeitman, J., Song, Z.-D., Regnault, N. & Bernevig, B. A. Hofstadter Topology: Noncrystalline Topological Materials at High Flux. *Physical Review Letters* **125**, 236804 (2020).
- [43] Zhu, J., Su, J.-J. & MacDonald, A. Voltage-Controlled Magnetic Reversal in Orbital Chern Insulators. *Physical Review Letters* **125**, 227702 (2020).

- [44] Polshyn, H. *et al.* Electrical switching of magnetic order in an orbital Chern insulator. *Nature* **588**, 66–70 (2020).
- [45] Zheng, Z. *et al.* Unconventional ferroelectricity in moiré heterostructures. *Nature* **588**, 71–76 (2020).
- [46] Wang, L. *et al.* One-Dimensional Electrical Contact to a Two-Dimensional Material. *Science* **342**, 614–617 (2013).
- [47] Adak, P. C. *et al.* Experimental data for "Electric field drives Chern transition in Hofstadter bands of twisted double bilayer graphene". *Zenodo* (2021). <https://doi.org/10.5281/zenodo.5653688> (2021).

Acknowledgements

We thank Justin C W Song, Allan H MacDonald, Ajit C Balram, and G J Sreejith for helpful discussions. We acknowledge Nanomission grant SR/NM/NS-45/2016 and DST SUPRA SPR/2019/001247 grant along with Department of Atomic Energy of Government of India 12-R&D-TFR-5.10-0100 for support. K.W. and T.T. acknowledge support from the Elemental Strategy Initiative conducted by the MEXT, Japan (Grant Number JPMXP0112101001) and JSPS KAKENHI (Grant Numbers 19H05790 and JP20H00354). D.K.M. would like to acknowledge financial support from Agence Nationale de la Recherche (ANR project “Dirac3D”) under Grant No. ANR-17-CE30-0023. D.K.M. and H.A.F. acknowledge support from NSF Grant No. DMR-1914451 and the Research Corporation for Science Advancement through a Cottrell SEED award. H.A.F. further acknowledges the support of NSF Grant No. ECCS-1936406, and of the US-Israel Binational Science Foundation (Grant Nos. 2016130 and 2018726). A.K. acknowledges support from the SERB (Govt. of India) via sanction no. ECR/2018/001443, DAE (Govt. of India) via sanction no. 58/20/15/2019-BRNS, as well as MHRD (Govt. of India) via sanction no. SPARC/2018-2019/P538/SL. D.G. acknowledges the use of HPC facility at IIT Kanpur. D.G acknowledges the CSIR (Govt. of India) for financial support.

Author Contributions

P.C.A., S.S., Chandan, and L.D.V.S. fabricated the devices. P.C.A. and S.S. did the measurements and analyzed the data. S.L. and A.M. helped in fabrication. D.G, D.K.M, H.A.F., and A.K. did the theoretical calculations. K.W. and T.T. grew the hBN crystals. P.C.A., S.S., A.K., and M.M.D. wrote the manuscript with inputs from everyone. M.M.D. supervised the project.

Competing Interests

The authors declare no competing interests.

Materials & Correspondence

Correspondence and requests for materials should be addressed to M.M.D.

Supplementary Information

1 Calculation of TDBG band structure at zero magnetic field

The continuum Hamiltonian¹⁻⁷ for twisted $AB - AB$ double bilayer graphene at small twist angle θ is written in a 8×8 matrix in the basis of the sublattices of four graphene layers ($A_1, B_1, A_2, B_2, A_3, B_3, A_4, B_4$) as,

$$H_{AB-AB}^\xi = \begin{pmatrix} H_1^\xi(\mathbf{k}_1) & g^\dagger(\mathbf{k}_1) & 0 & 0 \\ g(\mathbf{k}_1) & \tilde{H}_1^\xi(\mathbf{k}_1) & U & 0 \\ 0 & U^\dagger & \tilde{H}_2^\xi(\mathbf{k}_2) & g(\mathbf{k}_2) \\ 0 & 0 & g^\dagger(\mathbf{k}_1) & H_2^\xi(\mathbf{k}_2) \end{pmatrix} + \begin{pmatrix} \frac{3V}{2}I_2 & & & \\ & \frac{V}{2}I_2 & & \\ & & -\frac{V}{2}I_2 & \\ & & & -\frac{3V}{2}I_2 \end{pmatrix} \quad (\text{S1})$$

where

$$H_l^\xi(\mathbf{k}) = \begin{pmatrix} 0 & -\hbar v_F k_-^{\xi,l} \\ -\hbar v_F k_+^{\xi,l} & \Delta \end{pmatrix} \quad \tilde{H}_l^\xi(\mathbf{k}) = \begin{pmatrix} \Delta & -\hbar v_F k_-^{\xi,l} \\ -\hbar v_F k_+^{\xi,l} & 0 \end{pmatrix} \quad (\text{S2})$$

are the monolayer graphene Hamiltonians and

$$g(\mathbf{k}) = \begin{pmatrix} \hbar v_4 k_+^{\xi,l} & \gamma_1 \\ \hbar v_3 k_-^{\xi,l} & \hbar v_4 k_+^{\xi,l} \end{pmatrix} \quad (\text{S3})$$

is the intra-bilayer coupling Hamiltonian. Here, $k_\pm^{\xi,l} = e^{i\eta^{\xi,l}}(\xi k_x \pm i k_y)$ with $\eta^{1/2} = \mp\theta/2$. $\xi = \pm 1$ for \mathbf{K} and \mathbf{K}' valley respectively. v_3, v_4 are the velocities capturing the effect of the trigonal warping and electron-hole asymmetry respectively. Δ is the on-site potential felt by the vertically aligned lattice sites in the AB stacked bilayers and γ_1 is the coupling between the same sites. The tunneling matrix incorporating the twist between layers 2 and 3 is given by

$$U = \begin{pmatrix} t_0\alpha(\mathbf{r}) & t_1\beta(\mathbf{r}) \\ t_1\gamma(\mathbf{r}) & t_0\alpha(\mathbf{r}) \end{pmatrix}, \quad (\text{S4})$$

with $\alpha(\mathbf{r}) = \sum_{n=0}^2 \exp(-i\xi \mathbf{G}_n \cdot \mathbf{r})$, $\beta(\mathbf{r}) = \sum_{n=0}^2 (w^n)^\xi \exp(-i\xi \mathbf{G}_n \cdot \mathbf{r})$, $\gamma(\mathbf{r}) = \sum_{n=0}^2 (w^{*n})^\xi \exp(-i\xi \mathbf{G}_n \cdot \mathbf{r})$ and $w = \exp(i2\pi/3)$. \mathbf{G}_n are the reciprocal lattice vectors of the moiré lattice, given by $\mathbf{G}_0 = 0$, $\mathbf{G}_1 = k_\theta(-\sqrt{3}/2, 3/2)$ and $\mathbf{G}_2 = k_\theta(\sqrt{3}/2, 3/2)$, and $k_\theta = |\mathbf{K}_2 - \mathbf{K}_3|$, where \mathbf{K}_2 and \mathbf{K}_3 denote the locations of Dirac points of layers 2 and 3 respectively with respect to a common origin. V is the applied electrostatic potential and I_2 is the 2×2 unit matrix. We use $t_0 = 0.05$ eV, $t_1 = 0.085$ eV, $\gamma_1 = 0.4$ eV, $\Delta = 0.05$ eV, $v_3 = 1.036 \times 10^5$ m/s, $v_4 = 0.143 \times 10^5$ m/s.

2 Calculation of Hofstadter energy spectra in TDBG

In presence of a perpendicular magnetic field $\mathbf{B} = B\hat{z}$, the wave function^{8,9} of monolayer graphene at \mathbf{K} and \mathbf{K}' valley becomes,

$$\Psi_{n,\mathbf{K}} = c_n e^{-i\mathbf{K}_l \cdot \mathbf{r}} e^{-iXy/l_B^2} \frac{1}{\sqrt{L_y}} \begin{pmatrix} -i \operatorname{sgn}(n) \phi_{|n|-1}(x-X) \\ \phi_{|n|}(x-X) \end{pmatrix} \quad (\text{S5})$$

$$\Psi_{n,\mathbf{K}'} = c_n e^{-i\mathbf{K}'_l \cdot \mathbf{r}} e^{-iXy/l_B^2} \frac{1}{\sqrt{L_y}} \begin{pmatrix} \phi_{|n|}(x-X) \\ -i \operatorname{sgn}(n) \phi_{|n|-1}(x-X) \end{pmatrix} \quad (\text{S6})$$

and the corresponding Landau level energy is, $\varepsilon_n = \frac{\hbar v_F}{l} \operatorname{sgn}(n) \sqrt{2|n|}$.

Here $\phi_{|n|}(x-X) = (2^n n! \sqrt{\pi} l_B)^{-1/2} e^{-\frac{(x-X)^2}{2l_B^2}} H_n\left(\frac{x-X}{l_B}\right)$, $H_n(\cdot)$ being the Hermite polynomial of order n . $X = -k_y l_B^2$ is the guiding center coordinate, $l_B = \left(\frac{\Phi_0}{2\pi B}\right)^{1/2}$ is the magnetic length scale. The normalization coefficient is $c_n = 1$ for $n = 0$ and $c_n = \frac{1}{\sqrt{2}}$ for $n \neq 0$. \mathbf{K}_l are the moiré Dirac points associated with each layer.

The diagonal elements of the matrix Hamiltonian are,

$$\langle n, X, \nu | H^d | n', X', \nu' \rangle = \varepsilon_n \delta_{n,n'} \delta_{X,X'} \delta_{\nu,\nu'} \quad (\text{S7})$$

where $|n, X, \nu\rangle$ denotes the n -th Landau level of the ν layer with its guiding center localized around X .

The intra-bilayer matrix elements (for \mathbf{K} valley) are

$$\begin{aligned} \langle n, X, \nu | g(\mathbf{k})^\dagger | n', X', \nu' \rangle = c_n c_{n'} \left[-i \operatorname{sgn}(nn') \frac{\sqrt{2}}{l_B} \hbar v_4 \sqrt{|n'| - 1} \delta_{|n|, |n'|-1} - \operatorname{sgn}(n) \frac{\sqrt{2}}{l_B} \hbar v_3 \sqrt{|n'| + 1} \delta_{|n|, |n'+2} \right. \\ \left. - i \operatorname{sgn}(n') \gamma \delta_{|n|, |n'|-1} - i \frac{\sqrt{2}}{l_B} \hbar v_4 \sqrt{|n'|} \delta_{|n|, |n'|-1} \right] \delta_{X, X'} \delta_{\nu, 1} \delta_{\nu', 2}. \end{aligned} \quad (\text{S8})$$

The inter-bilayer matrix elements (for \mathbf{K} valley) are found to be,

$$\begin{aligned} \langle n, X, \nu | U | n', X', \nu' \rangle = \left[\delta_{X, X' - k_\theta l_B^2} A_{n, n'} e^{-iG'_{0,x}(X+X')/2} + \delta_{X, X' + k_\theta l_B^2/2} B_{n, n'} e^{-iG'_{1,x}(X+X')/2} \right. \\ \left. + \delta_{X, X' + k_\theta l_B^2/2} D_{n, n'} e^{-iG'_{2,x}(X+X')/2} \right] \delta_{\nu, 2} \delta_{\nu', 3} \end{aligned} \quad (\text{S9})$$

where $\mathbf{G}'_i = \mathbf{G}_i - k_\theta \hat{y}$.

The functions,

$$\begin{aligned} A_{n, n'} = c_n c_{n'} \left[t_0 \operatorname{sgn}(nn') f_{|n|-1, |n'|-1}(\mathbf{G}'_0) + t_0 f_{|n|, |n'|}(\mathbf{G}'_0) + it_1 \operatorname{sgn}(n) f_{|n|-1, |n'|}(\mathbf{G}'_0) \right. \\ \left. - it_1 \operatorname{sgn}(n') f_{|n|, |n'|-1}(\mathbf{G}'_0) \right], \end{aligned} \quad (\text{S10})$$

$$\begin{aligned} B_{n, n'} = c_n c_{n'} \left[t_0 \operatorname{sgn}(nn') f_{|n|-1, |n'|-1}(\mathbf{G}'_1) + t_0 f_{|n|, |n'|}(\mathbf{G}'_1) + it_1 w \operatorname{sgn}(n) f_{|n|-1, |n'|}(\mathbf{G}'_1) \right. \\ \left. - it_1 w^* \operatorname{sgn}(n') f_{|n|, |n'|-1}(\mathbf{G}'_1) \right] \end{aligned} \quad (\text{S11})$$

$$\begin{aligned} D_{n, n'} = c_n c_{n'} \left[t_0 \operatorname{sgn}(nn') f_{|n|-1, |n'|-1}(\mathbf{G}'_2) + t_0 f_{|n|, |n'|}(\mathbf{G}'_2) + i \operatorname{sgn}(n) t_1 w^* f_{|n|-1, |n'|}(\mathbf{G}'_2) \right. \\ \left. - it_1 \operatorname{sgn}(n') w f_{|n|, |n'|-1}(\mathbf{G}'_2) \right] \end{aligned} \quad (\text{S12})$$

involve overlap between quantum states with different guiding centers and,

$$f_{n,n'}(\mathbf{G}) = \sqrt{\frac{m!}{M!}} \left(\frac{-G_x - iG_y}{|\mathbf{G}|} \right)^{n'-n} \left(i|\mathbf{G}|l_B/\sqrt{2} \right)^{|n-n'|} e^{-|\mathbf{G}|^2 l_B^2/4} L_m^{|n-n'|} (|\mathbf{G}|^2 l_B^2/2) \quad (\text{S13})$$

with $L_m^a(x)$ is an associated Laguerre polynomial and $m = \min(n, n')$, $M = \max(n, n')$.

It can be seen that the inter-bilayer Hamiltonian U couples quantum states with different guiding centers separated by $k_\theta l_B^2/2$. The information about the relative twist angle between the two bilayers thus gets encoded in the coupling between different guiding centers.

The full matrix Hamiltonian⁹⁻¹¹ for the \mathbf{K} valley can be written as,

$$H_{\mathbf{K}} = \sum_{n,n',X,X',\nu,\nu'} h(n, X, \nu|n', X', \nu') a_{n,X,\nu}^\dagger a_{n',X',\nu'} \quad (\text{S14})$$

where,

$$\begin{aligned} h(n, X, \nu|n', X', \nu') = & \varepsilon_n \delta_{n,n'} \delta_{X,X'} \delta_{\nu,\nu'} + c_n c_{n'} \delta_{X,X'} \left[-i \operatorname{sgn}(nn') \frac{\sqrt{2}}{l_B} \hbar v_4 \sqrt{|n'| - 1} \delta_{|n|,|n'|-1} \right. \\ & - \operatorname{sgn}(n) \frac{\sqrt{2}}{l_B} \hbar v_3 \sqrt{|n'| + 1} \delta_{|n|,|n'+2} - i \operatorname{sgn}(n') \gamma \delta_{|n|,|n'|-1} \\ & \left. - i \frac{\sqrt{2}}{l_B} \hbar v_4 \sqrt{|n'|} \delta_{|n|,|n'|-1} \right] \delta_{\nu,1} \delta_{\nu',2} + \delta_{\nu,2} \delta_{\nu',3} \left[\delta_{X,X'-k_\theta l_B^2} A_{n,n'} e^{-iG'_{0,x}(X+X')/2} \right. \\ & \left. + \delta_{X,X'+k_\theta l_B^2/2} B_{n,n'} e^{-iG'_{1,x}(X+X')/2} + \delta_{X,X'+k_\theta l_B^2/2} D_{n,n'} e^{-iG'_{2,x}(X+X')/2} \right] + \text{h.c.} \end{aligned} \quad (\text{S15})$$

Similarly, we can find the matrix Hamiltonian for \mathbf{K}' valley.

Notice that the Hamiltonian in Eq. (S14) can be made to be periodic, i.e.,

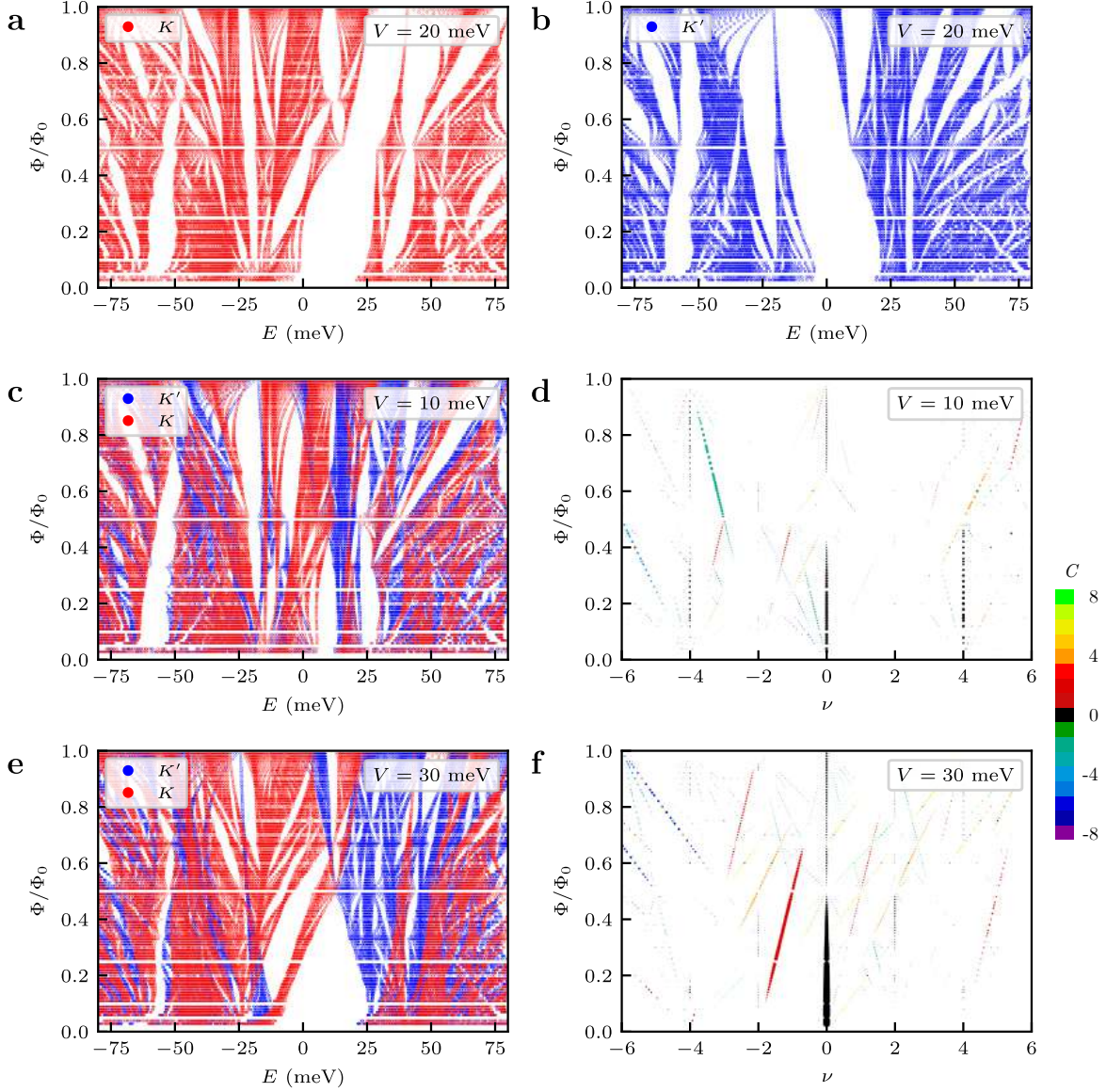
$$h(n, X, \nu|n', X', \nu') = h(n, X + \Delta X, \nu|n', X' + \Delta X, \nu') \quad (\text{S16})$$

if $\Delta X = qk_\theta l_B^2/2$ where q is an integer. The above condition of discrete translational symmetry of the Hamiltonian can also be rewritten as,

$$\frac{q}{p} = \frac{6\phi}{\phi_0} \quad (\text{S17})$$

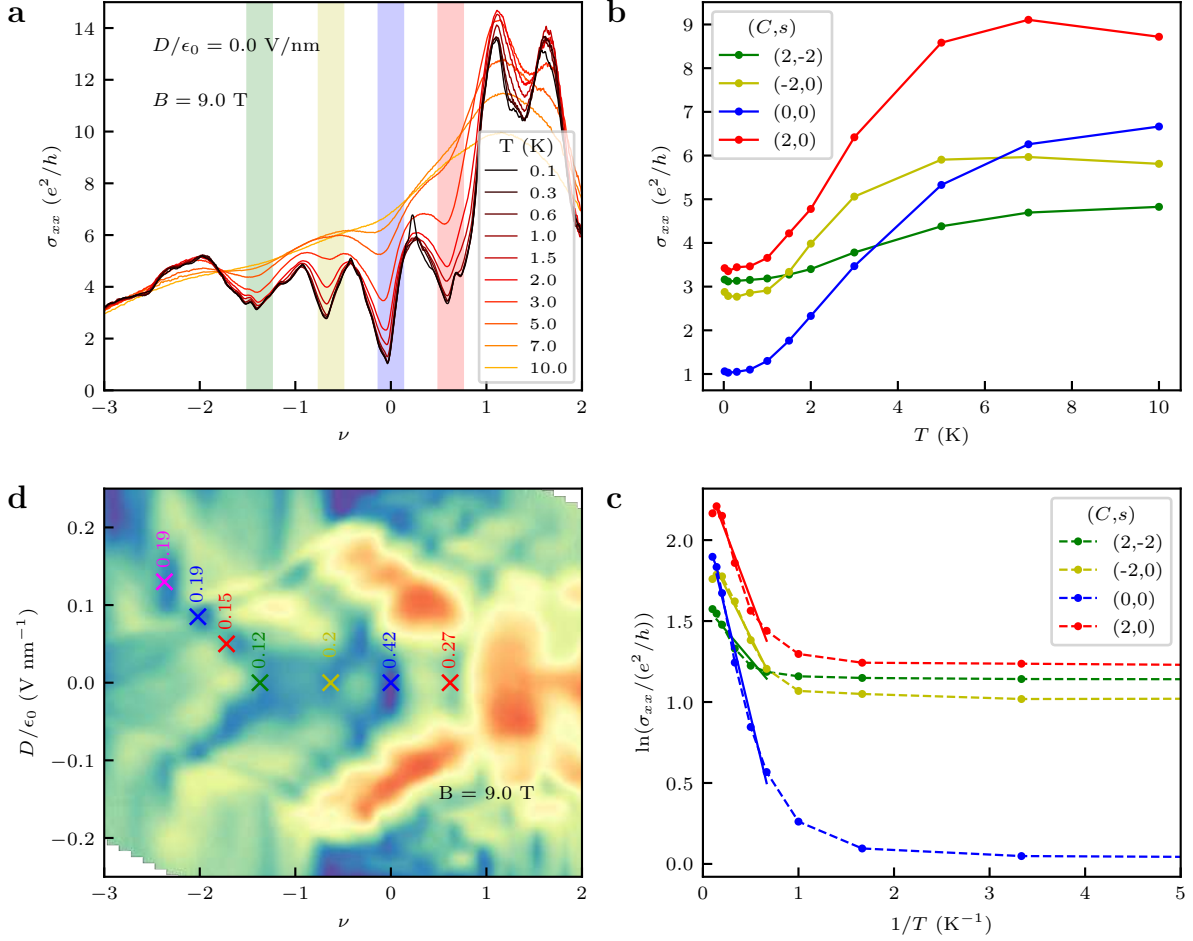
where p is an integer mutually coprime to q and ϕ_0 is the flux quantum. This equation is basically the condition that a moiré unit cell contains a rational fraction of the flux quantum. The size of the matrix that we need to diagonalize is $4 \times q \times N_{LL}$, N_{LL} is the number of Landau levels of monolayer graphene. One requires a cutoff for the number of Landau levels in performing the numerical calculation. We choose this cutoff such that the energy spectrum and the gaps found in the low energy sector does not change with further increase of Landau levels. As we go to lower magnetic flux per unit cell, we require larger cutoff. The minimum number of Landau levels we have used is 31 when the magnetic flux per unit cell is close to 1. We have used 151 Landau levels when the magnetic flux ϕ/ϕ_0 is lower than 0.1.

As discussed in the main manuscript, our theoretical calculations capture the experimental results very well. While we see some small quantitative disagreement, we attribute that to the extra potential on each layer in a realistic sample induced by the presence of other layers. As a result, the effective potential on each layer could be different from the applied potential. In principle, a self-consistent calculation could capture the actual potential present in the layers. While such computation is numerically quite expensive, the resulting solutions will simply differ by certain shifts of potential.



Supplementary Figure 1: Calculated Hofstadter spectra and Wannier diagrams for TDBG with twist angle 1.10° a,b, Hofstadter spectra of K and K' valleys, respectively, for an interlayer potential of $V = 20$ meV. The spectra combined from both valleys is shown in Fig. 3a in the main text with corresponding Wannier diagram in Fig. 3b. c,e, Hofstadter spectra considering both K and K' valleys for $V = 10$ meV and 30 meV, respectively. d,f, Wannier diagrams extracted from c and e.

3 Extraction of Hofstadter gaps from experimental data



Supplementary Figure 2: Estimation of LL gaps. **a**, Variation of σ_{xx} vs. ν for different values of temperature at $B = 9$ T and $D/\epsilon_0 = 0$ V/nm. **b**, Temperature dependence of σ_{xx} minima for four different LL gaps at $B = 9$ T and $D/\epsilon_0 = 0$ V/nm extracted from **a**. **c**, Extraction of LL gap by fitting the linear region in $\ln \sigma_{xx}$ vs. $1/T$ plots obtained from **b**. Solid lines represent the linear fit. **d**, Values of extracted LL gaps in meV at some points in ν - D parameter space at $B = 9$ T.

To estimate the Hofstadter gaps we measure the variation of σ_{xx} as a function of ν for different temperatures at a constant magnetic field as shown in Supplementary Fig. 2a. Then we identified the σ_{xx} minima corresponding to the Chern gaps and plot the σ_{xx} magnitude as a function of temperature (T) for different Chern gaps as shown in Supplementary Fig. 2b. Now by fitting Arrhenius activation formula $\sigma_{xx} \propto \exp\{-\Delta_g/(2k_B T)\}$ to the linear region in σ_{xx} vs $1/T$ curve we extract the gap Δ_g of the corresponding Chern gaps (see Supplementary Fig. 2c). Here, k_B is the Boltzmann constant. We repeat the analysis for different values of D and summarize the extracted

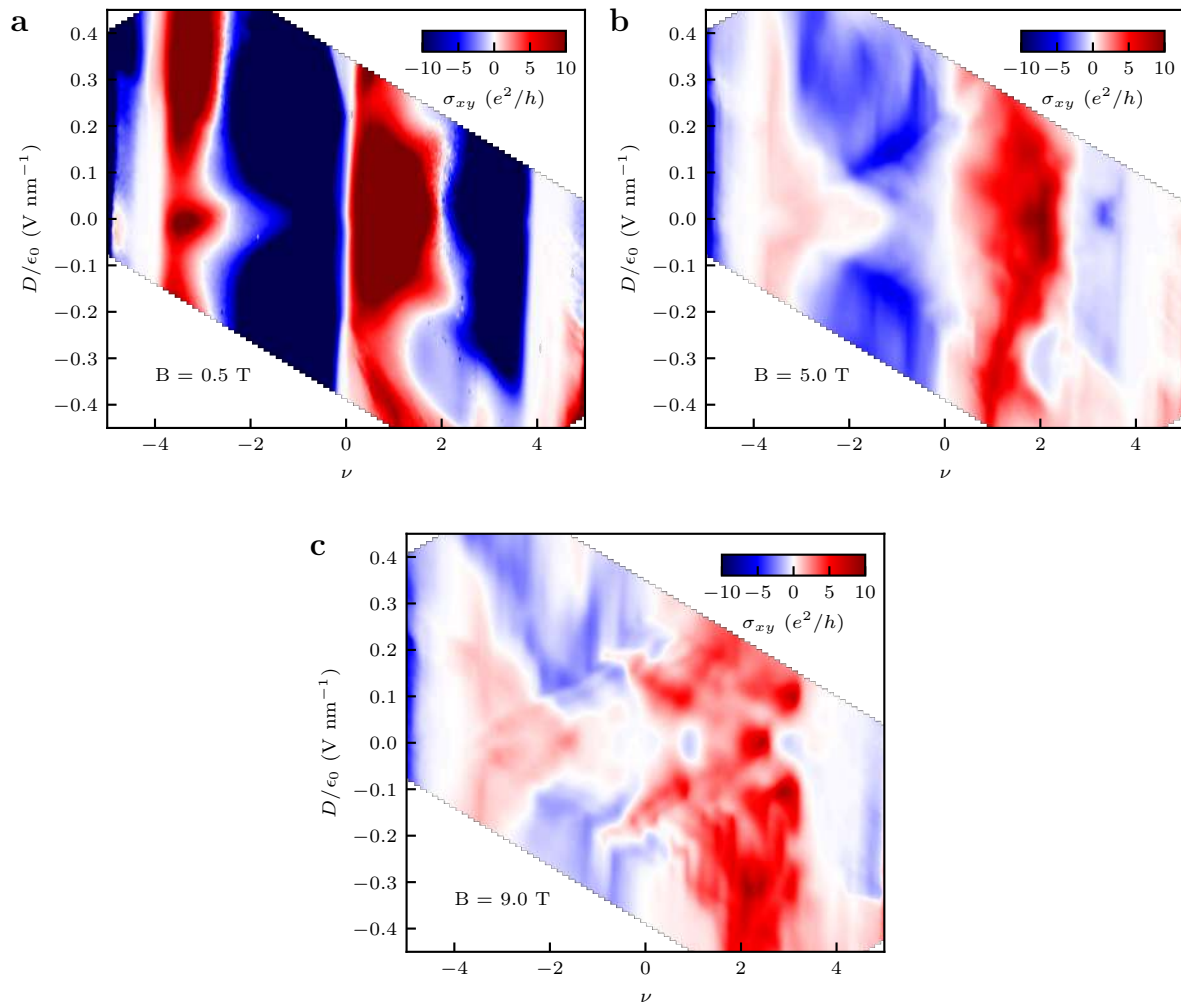
gap at different (ν, D) points in Supplementary Fig. 2d.

4 Additional magneto-transport data

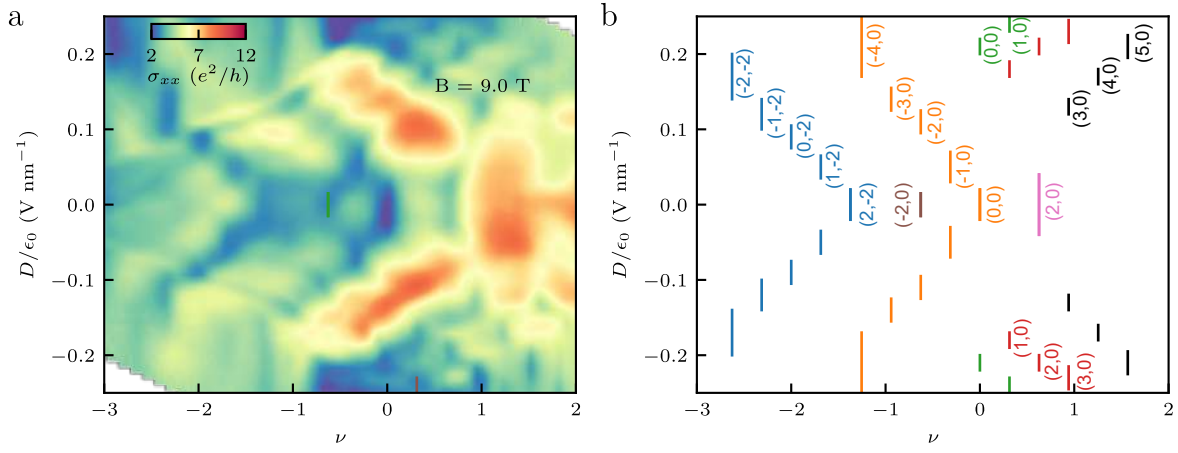
In Supplementary Fig. 3, we show the color-scale plots of σ_{xy} as a function of ν and D for three different values of B . The corresponding color-scale plots of σ_{xx} are shown in Fig. 1 in the main text. In Supplementary Fig. 4, we have marked additional Chern gaps with values of (C, s) corresponding to the same data used in Fig. 2a in the main text. Here, C is the Chern number and s is an integer denoting the moiré filling factor corresponding to the number of carriers per moiré unit cell in zero magnetic field.

Supplementary Fig. 5b and 5c show ν lineslices of the σ_{xx} and the corresponding σ_{xy} across the $s = -2$ and $s = 0$ Chern gaps at fixed magnetic fields. A dip in σ_{xx} in the blue-shaded region shows a (C, s) Chern gap. Measured values of σ_{xy} is close to Ce^2/h for each of the (C, s) Chern states showing approximate quantization. As mentioned in the main text, we do not see a clear quantization in σ_{xy} for all (C, s) states possibly due to small values of Hofstadter gaps and twist angle-inhomogeneity disorder. In Supplementary Note 6, we have discussed the role of flat bands in setting small Hofstadter gaps.

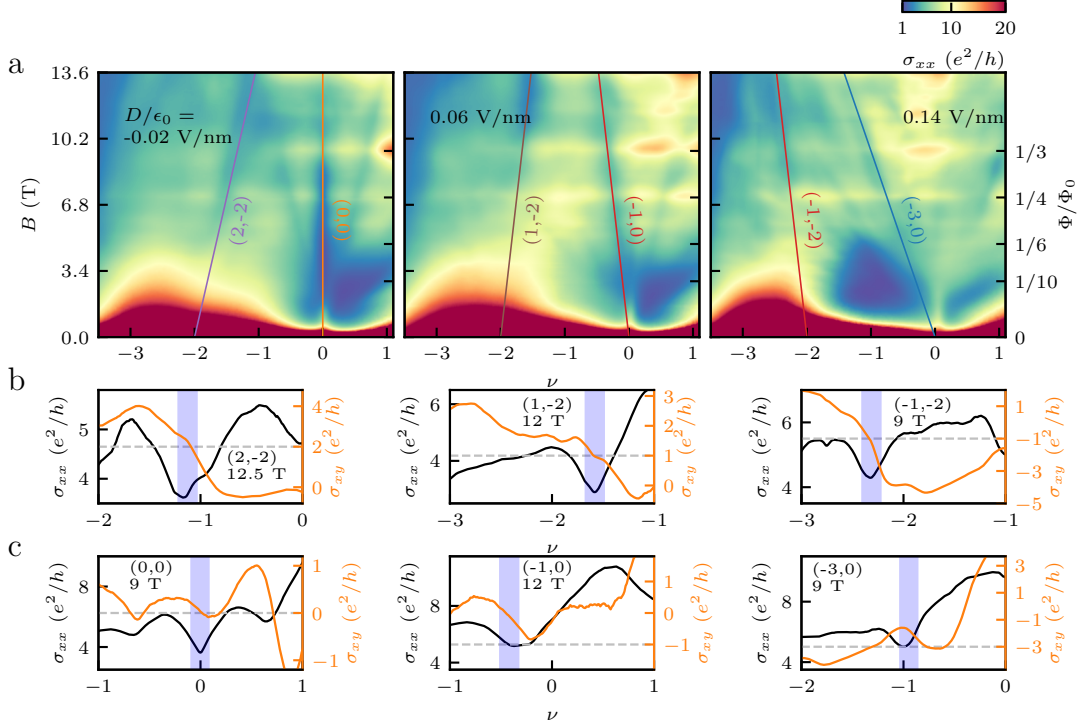
We observe electric field tunable Chern gaps across a wide range of twist angles ($1.09^\circ - 1.46^\circ$) in multiple devices. In the main text and in Supplementary Figs. 3-6, we have used a device with twist angle 1.10° (device 1). In Supplementary Fig. 6, we show the details of fittings to extract the (C, s) states. In Supplementary Fig. 7, we show the evolution of Chern gaps from another device (device 2) with a twist angle of 1.09° . Though some of the Chern gaps are not fully developed possibly due to twist-angle disorder, the evolution of Chern gaps is overall similar to the data from device 1 in Supplementary Fig. 4. Supplementary Fig. 8 shows data from device 3 with a twist angle of 1.46° . In this device, we clearly see a correlated gap at $\nu = 2$ at zero magnetic field, as seen in Supplementary Fig. 8b. From Supplementary Fig. 8c-d, we see Chern gaps that tunes with the electric field. Observation of tunable Chern gaps is further repeated for another twist angle of 1.42° in Supplementary Fig. 9.



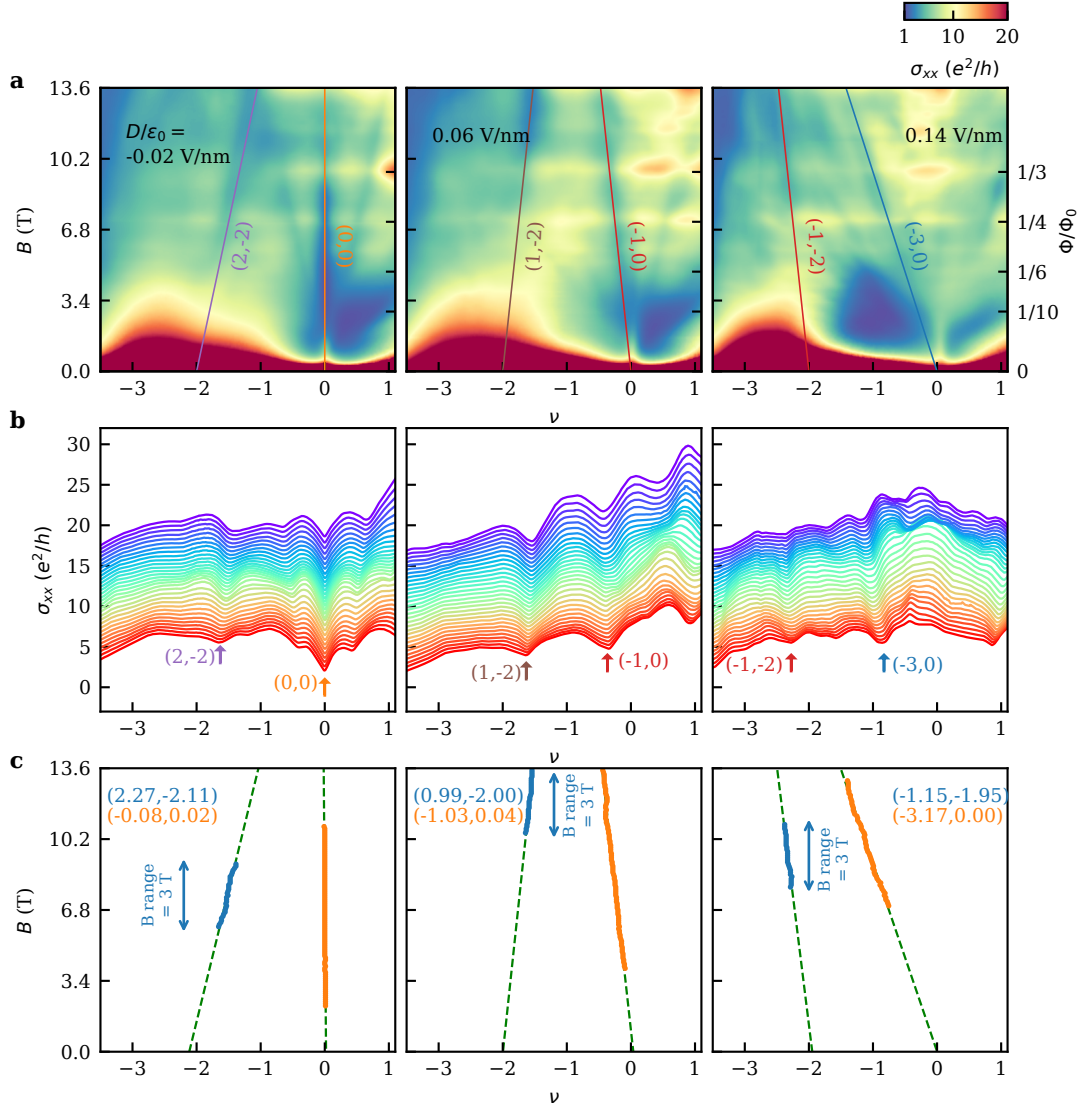
Supplementary Figure 3: Evolution of σ_{xy} . a,b,c, Color-scale plot of σ_{xy} vs. ν and D for three different values of magnetic field.



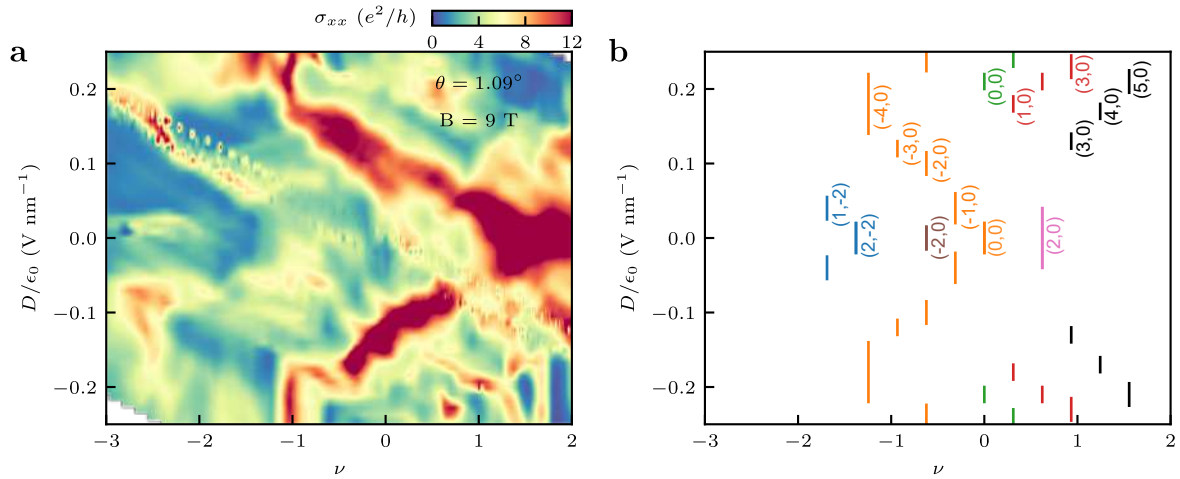
Supplementary Figure 4: Marking additional Chern gaps for device 1 with twist angle 1.10° used in the main text. **a**, Color-scale plot of σ_{xx} as a function D and ν at $B = 9$ T, as plotted in Fig. 2a of the main text, but without marking Chern gaps. **b**, The extracted values of (C, s) corresponding to σ_{xx} dips in **a**. Here, C is Chern number and s is an integer denoting the moiré filling factor corresponding to the number of carriers per moiré unit cell in zero magnetic field. The Chern gaps labeled with blue and orange colors are what we emphasized in the main text; here we have marked additional Chern gaps with different colors.



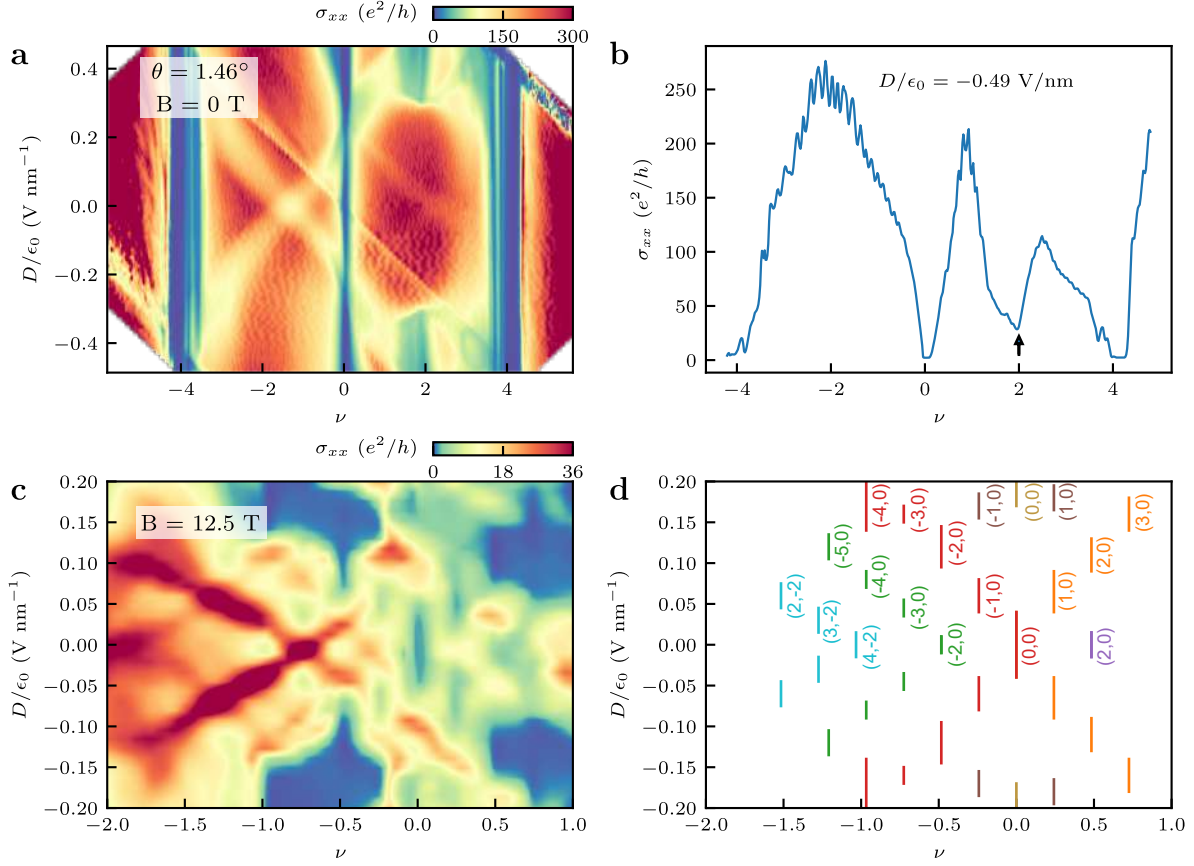
Supplementary Figure 5: Approximate quantization of (C, s) states. **a**, Fan diagrams reproduced from Fig. 2b of the main manuscript, with solid lines overlaid on σ_{xx} minimas, indicating the (C, s) Chern gaps. Line slices of σ_{xx} (black colored plot corresponding to the left axis) and σ_{xy} (orange colored plot corresponding to the right axis) vs. filling (ν) at fixed magnetic field for $s = -2$ (b) and $s = 0$ (c) Chern gaps. The dashed horizontal lines are a guide to the eye, corresponding to $\sigma_{xy} = Ce^2/h$. The blue-shaded ν window (with a width of 0.2) is centered at the ν value calculated from the Diophantine equation for a particular (C, s) state at that B value. σ_{xx} shows a dip within the blue ν -window due to each (C, s) Chern gap. The magnitude of measured σ_{xy} being close to the corresponding values of Ce^2/h in (b) and (c) shows approximate quantization.



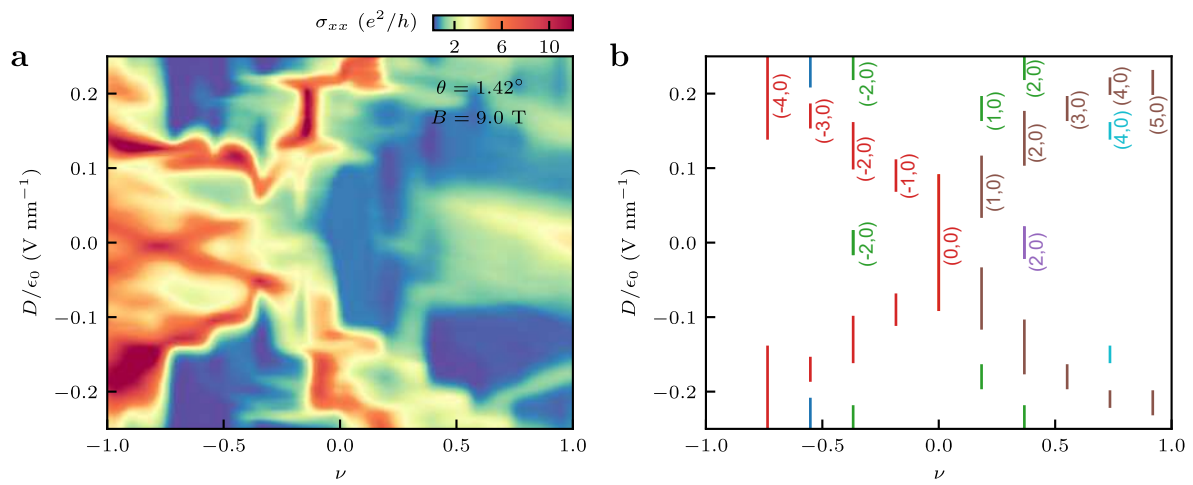
Supplementary Figure 6: Details of fitting to extract (C, s) for device 1 with twist angle 1.10° used in the main text. **a**, Fan diagrams reproduced from Fig. 2b of the main manuscript. **b**, σ_{xx} vs ν plots where magnetic field (B) is varied in steps of 0.1 T, showing clear minima in σ_{xx} corresponding to different (C, s) states as indicated by the arrows. The three different plots are for the three different electric fields used in **a**. Within a particular sub-panel, each σ_{xx} vs ν plot is shifted up by 0.5 units. **c**, Fitting of the extracted (ν, B) points of σ_{xx} minima for the different (C, s) states. The blue (orange) dots indicates σ_{xx} minima for $s = -2$ ($s = 0$) state. The extracted (C, s) values are indicated in each plot. The corresponding σ_{xx} vs ν plots from which the σ_{xx} minima for $s = -2$ states are extracted are shown in **b**. Thirty-one σ_{xx} vs ν slices are used to fit each $(C, s = -2)$ state.



Supplementary Figure 7: Electric field tunable Chern gaps from device 2 with twist angle 1.09°. **a**, Evolution of σ_{xx} at 9 T showing multiple peaks/dips corresponding to Chern gaps evolving with the electric field. **b**, Values of (C, s) corresponding to the σ_{xx} dips in **a**. Overall, the evolution is similar to that for device 1 (Supplementary Fig. 4).



Supplementary Figure 8: Correlated insulator state and electric field tunable Chern gaps from device 3 with twist angle 1.46° . **a**, σ_{xx} as a function of ν and D at zero magnetic field. Correlated gap appears at $\nu = 2$ for $|D|/\epsilon_0 \sim 0.4\text{ V/nm}$. **b**, A line slice at $D/\epsilon_0 = -0.49\text{ V/nm}$ clearly showing a dip in σ_{xx} at $\nu = 2$. **c**, Evolution of σ_{xx} at a finite magnetic field of 12.5 T showing multiple peaks/dips corresponding to Chern gaps evolving with the electric field. **d**, (C, s) values corresponding to the σ_{xx} dips in **c**.



Supplementary Figure 9: Electric field tunable Chern gaps from device 3 with twist angle 1.42°. **a**, Evolution of σ_{xx} at 9 T showing multiple peaks/dips corresponding to Chern gaps evolving with the electric field. **b**, (C, s) values corresponding to the σ_{xx} dips in **a**.

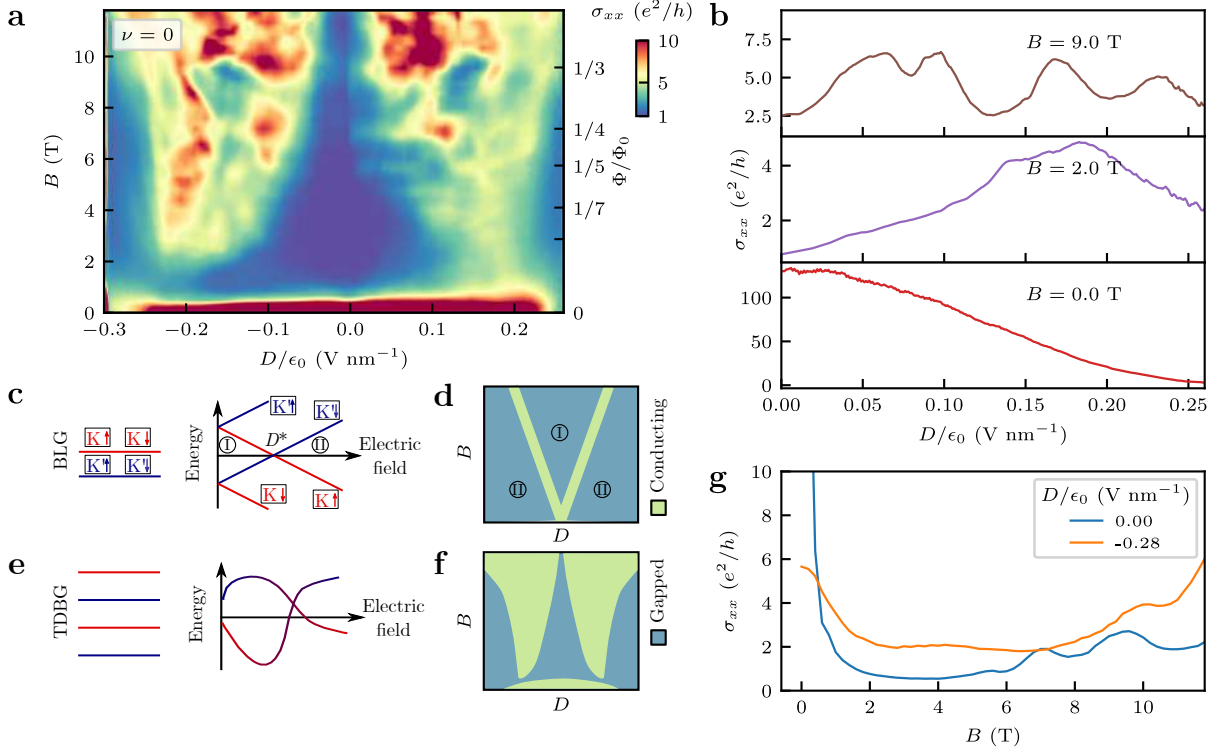
5 Evolution of the CNP gap and the role of tunable layer polarization

As discussed in the main text, the electric field tunable layer polarization plays an important role in TDBG. In particular, the tunable layer polarization can lead to multiple closings and reopening of a gap, as the energy levels disperse nonmonotonically with the electric field. To demonstrate this, in Supplementary Fig. 10a we show a color-scale plot of σ_{xx} at the CNP as a function of D and B from device 1. Few line slices of σ_{xx} vs. D at fixed values of B are shown in Supplementary Fig. 10b. For $B = 0$ T we note σ_{xx} remains high for $|D|/\epsilon_0 \lesssim 0.23$ V/nm suggesting that CNP gap opens up only after a finite electric field. However, at a moderate magnetic field above 2 T, σ_{xx} becomes small with a dip at $D = 0$, indicating the opening of the CNP gap even at zero electric field. At higher magnetic fields such as at $B = 9$ T, the CNP gap closes and reopens multiple times.

To examine the role of tunable layer polarization in TDBG we contrast with the case of BLG^{12,13}, where the occupied lowest LL's for $\nu = 0$ undergo a simple evolution over most of the range of D . As shown in the schematic of Supplementary Fig. 10c, electrons from $K(K')$ valleys occupy upper (lower) layer. At a finite B and low electric field (region I) the occupied states support spins in the two valleys which are antiferromagnetically correlated but cant into the magnetic field direction. However, as the electric field is increased, the energy of the LLs from opposite valleys disperse in opposite directions monotonically due to the layer-valley locking. This monotonic dispersion results in a near gap-closing at D^* , around which there may be other gapped or gapless phases in a narrow range of D due to interactions¹⁴⁻¹⁶. Outside this transition region a layer-polarized phase quickly emerges at higher electric fields (region II). The evolution of σ_{xx} in the parameter space of B and D for BLG is schematically shown in Supplementary Fig. 10d; the CNP gap in TBG shows similar evolution⁴⁰.

Now we turn to the case of TDBG which can be considered as two copies of BLG. In contrast to BLG, as shown in Supplementary Fig. 10e, a strong hybridization between the layers due to twisting ensures that the LLs from the two valleys do not fully layer-polarize in the same range of D as for BLG. The polarization varies as the electric field changes the hybridization, and consequently the nonmonotonic evolution of the LLs results in a complex evolution of the CNP gap as shown in Supplementary Fig. 10a and schematically in Supplementary Fig. 10f.

We further note the unique evolution of the CNP gap with B . Unlike BLG, where CNP gap is enhanced with B , TDBG shows a different trend. As seen in Supplementary Fig. 10g, σ_{xx} first decreases indicating the enhancement of the CNP gap with B . However, at high B , σ_{xx} increases indicating a gap closing. This is consistent with the Hofstadter energy spectrum for a topological band, where the gap with a nonzero Chern number C closes at $\Phi/\Phi_0 \leq 1/|C|$ ⁴¹.

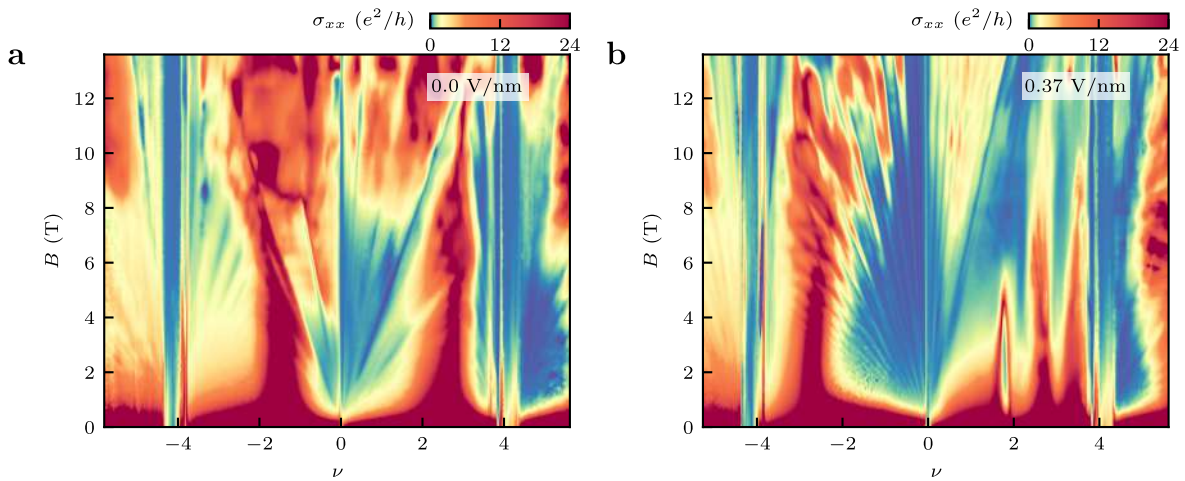


Supplementary Figure 10: Evolution of the CNP gap. **a**, Color-scale plot of σ_{xx} as a function D and B at $\nu = 0$. **b**, Line slices of σ_{xx} vs. D at $\nu = 0$ for few magnetic field values. **c**, Schematic showing the evolution of CNP gap in BLG from spin-polarized state (region I) to layer-polarized state (region II) as D is increased. The LLs from two valleys are locked to two layers and thus LL energy changes monotonically with D . **d**, Map of the gapped and conducting regions in the parameter space of B and D at CNP for BLG¹². **e**, In TDBG two copies of BLG are hybridized. Thus LLs from different valleys are not locked to any particular layer – layer polarization is varied with D . Tunable polarization results in nonmonotonic evolution of the energy levels giving rise to multiple closing and reopening of the gap. **f**, A simplified schematic version of **a** to contrast the evolution of the CNP gap with that in BLG. **g**, Line slices from **a** showing σ_{xx} vs. B at $\nu = 0$ for two electric field values. The evolution of σ_{xx} indicates that the CNP gap first increases and then decreases as B is increased suggesting gap opening and closing as a function of B .

6 Role of flat band energy scale on resolving Hofstadter spectra

The narrow bandwidth of the flat bands sets a small energy scale in TDBG, resulting in small values of the Hofstadter gaps. To understand the effect of flat band, we plot two fan diagrams for two

different values of D from device 3 with a twist angle of 1.46° in Supplementary Fig. 11. We find that the fan diagram for higher magnitude of electric field has more number of resolved Hofstadter gaps, consistent with the fact that the bandwidth of the flat bands increases with the electric field magnitude in TDBG³⁰. Furthermore, we observe more number of Hofstadter gaps resolved on the hole side of the fan diagram, as seen in Supplementary Fig. 11b. This is because the bandwidth of the valence flat band is higher than that of the conduction flat band, as reflected in the observation of $\nu = 2$ correlated gap only on the electron side (see Supplementary Fig. 8).



Supplementary Figure 11: Role of flat band energy scale on resolving Hofstadter spectra. **a-b**, Fan diagrams from device 3 with twist angle 1.46° for two different values of D : 0.0 V/nm (**a**) and 0.37 V/nm (**b**). More gaps are resolved for higher electric field due to higher bandwidth.

References

- [1] Bistritzer, R. & MacDonald, A. H. Moiré bands in twisted double-layer graphene. *Proceedings of the National Academy of Sciences* **108**, 12233–12237 (2011).
- [2] Lopes dos Santos, J. M. B., Peres, N. M. R. & Castro Neto, A. H. Graphene bilayer with a twist: Electronic structure. *Phys. Rev. Lett.* **99**, 256802 (2007).
- [3] Lopes dos Santos, J. M. B., Peres, N. M. R. & Castro Neto, A. H. Continuum model of the twisted graphene bilayer. *Phys. Rev. B* **86**, 155449 (2012).
- [4] Koshino, M. Band structure and topological properties of twisted double bilayer graphene. *Phys. Rev. B* **99**, 235406 (2019).
- [5] Chebroly, N. R., Chittari, B. L. & Jung, J. Flat bands in twisted double bilayer graphene. *Phys. Rev. B* **99**, 235417 (2019).
- [6] Moon, P. & Koshino, M. Optical absorption in twisted bilayer graphene. *Phys. Rev. B* **87**, 205404 (2013).
- [7] Koshino, M. & Moon, P. Electronic properties of incommensurate atomic layers. *Journal of the Physical Society of Japan* **84**, 121001 (2015).
- [8] Moon, P. & Koshino, M. Energy spectrum and quantum hall effect in twisted bilayer graphene. *Phys. Rev. B* **85**, 195458 (2012).
- [9] Crosse, J. A., Nakatsuji, N., Koshino, M. & Moon, P. Hofstadter butterfly and the quantum hall effect in twisted double bilayer graphene. *Phys. Rev. B* **102**, 035421 (2020).
- [10] Bistritzer, R. & MacDonald, A. H. Moiré butterflies in twisted bilayer graphene. *Phys. Rev. B* **84**, 035440 (2011).
- [11] Hejazi, K., Liu, C. & Balents, L. Landau levels in twisted bilayer graphene and semiclassical orbits. *Physical Review B* **100**, 035115 (2019).
- [12] Weitz, R. T., Allen, M. T., Feldman, B. E., Martin, J. & Yacoby, A. Broken-Symmetry States in Doubly Gated Suspended Bilayer Graphene. *Science* **330**, 812–816 (2010).

- [13] Kim, S., Lee, K. & Tutuc, E. Spin-polarized to valley-polarized transition in graphene bilayers at $\nu = 0$ in high magnetic fields. *Physical Review Letters* **107**, 016803 (2011).
- [14] Hunt, B. M. *et al.* Direct measurement of discrete valley and orbital quantum numbers in bilayer graphene. *Nature Communications* **8**, 948 (2017).
- [15] Murthy, G., Shimshoni, E. & Fertig, H. A. Spin-valley coherent phases of the $\nu = 0$ quantum hall state in bilayer graphene. *Phys. Rev. B* **96**, 245125 (2017).
- [16] Li, J. *et al.* Metallic phase and temperature dependence of the $\nu = 0$ quantum hall state in bilayer graphene. *Phys. Rev. Lett.* **122**, 097701 (2019).